Monthly Notices
of the
ROYAL ASTRONOMICAL SOCIETY

MNRAS **490,** 5335–5352 (2019)
Advance Access publication 2019 October 12

doi:10.1093/mnras/stz2861

# The K2-HERMES Survey: age and metallicity of the thick disc

Sanjib Sharma [1,2]★ Dennis Stello,[1,2,3,4] Joss Bland-Hawthorn [1,2] Michael R. Hayden,[1,2] Joel C. Zinn,[5] Thomas Kallinger,[6] Marc Hon [3] Martin Asplund,[2,7] Sven Buder [8]† Gayandhi M. De Silva,[9] Valentina D'Orazi [10] Ken Freeman,[7] Janez Kos,[11] Geraint F. Lewis [1] Jane Lin,[7] Karin Lind,[8,12] Sarah Martell [2,3] Jeffrey D. Simpson [3] Rob A. Wittenmyer,[13] Daniel B. Zucker,[9,14] Tomaz Zwitter [11] Timothy R. Bedding [1] Boquan Chen,[1] Klemen Cotar [11] James Esdaile,[3] Jonathan Horner,[13] Daniel Huber,[15,16,17] Prajwal R. Kafle,[18] Shourya Khanna [1] Tanda Li [1] Yuan-Sen Ting,[19,20,21] David M. Nataf,[22] Thomas Nordlander [2,7] Mohd Hafiz Mohd Saadon,[3] Gregor Traven,[11] Duncan Wright[13] and Rosemary F. G. Wyse[22]

*Affiliations are listed at the end of the paper*

Accepted 2019 September 27. Received 2019 September 16; in original form 2019 April 28

## ABSTRACT

Asteroseismology is a promising tool to study Galactic structure and evolution because it can probe the ages of stars. Earlier attempts comparing seismic data from the *Kepler* satellite with predictions from Galaxy models found that the models predicted more low-mass stars compared to the observed distribution of masses. It was unclear if the mismatch was due to inaccuracies in the Galactic models, or the unknown aspects of the selection function of the stars. Using new data from the K2 mission, which has a well-defined selection function, we find that an old metal-poor thick disc, as used in previous Galactic models, is incompatible with the asteroseismic information. We use an importance-sampling framework, which takes the selection function into account, to fit for the metallicities of a population synthesis model using spectroscopic data. We show that spectroscopic measurements of [Fe/H] and [$\alpha$/Fe] elemental abundances from the GALAH survey indicate a mean metallicity of $\log(Z/Z_\odot) = -0.16$ for the thick disc. Here $Z$ is the effective solar-scaled metallicity, which is a function of [Fe/H] and [$\alpha$/Fe]. With the revised disc metallicities, for the first time, the theoretically predicted distribution of seismic masses show excellent agreement with the observed distribution of masses. This indirectly verifies that the asteroseismic mass scaling relation is good to within five per cent. Assuming the asteroseismic scaling relations are correct, we estimate the mean age of the thick disc to be about 10 Gyr, in agreement with the traditional idea of an old $\alpha$-enhanced thick disc.

**Key words:** methods: data analysis – methods: numerical – Galaxy: stellar content – Galaxy: structure.

## 1 INTRODUCTION

In recent years, asteroseismology has emerged as a powerful tool to study Galactic structure and evolution (Miglio et al. 2009; Chaplin et al. 2011b; Miglio et al. 2013; Casagrande et al. 2014, 2016; Sharma et al. 2016, 2017; Anders et al. 2017; Rodrigues et al. 2017; Silva Aguirre et al. 2018). However, previous attempts based on data from the original *Kepler* mission (Borucki et al. 2010), which was designed for detecting transiting planets, have struggled to match the predictions of stellar-population-synthesis Galactic models to observations, with the models producing too many low mass stars (Sharma et al. 2016, 2017). There are three possible causes for this

★ E-mail: sanjib.sharma@sydney.edu.au
† Fellow of the International Max Planck Research School for Astronomy & Cosmic Physics at the University of Heidelberg.

© 2019 The Author(s)
Published by Oxford University Press on behalf of the Royal Astronomical Society

Downloaded from https://academic.oup.com/mnras/article/490/4/5335/5586605 by guest on 07 December 2020

mismatch: (i) inaccuracies in the adopted selection function of the observed stars, (ii) an incorrect Galactic model, and (iii) systematics in the scaling relations used to relate asteroseismic observables ($\Delta\nu$, $\nu_{\rm max}$) to density and surface gravity of the stars. The first cause can be eliminated using data from the K2 Galactic Archaeology Program (K2GAP, Stello et al. 2015, 2017), which observes oscillating giants with the 'second-life' *Kepler* mission (K2, Howell et al. 2014) following a well-defined selection function. In this paper we therefore, first use the K2GAP data to test if predictions of the Galactic models that are constrained independently of the asteroseismic data match the observed asteroseismic data. This provides an indirect way to test the scaling relations. Having shown that the scaling relations are fairly accurate, next, we use them in combination with the asteroseismic data to fit some of the parameters in the Galactic model, and discuss the implications for our understanding of the Galaxy. Unlike for *Kepler*, however, the seismic detection completeness of K2 is not 100 per cent. This is because the time span of K2 light curves (typically 80 d) is much shorter than for *Kepler* (typically more than a year). Hence, we carefully study the detection completeness in K2, and devise ways to take them into account when comparing observations to models.

In a Galactic model, the mass distributions of giants are sensitive to the age and the metallicity of the stellar populations in the model. While the role of age was investigated in Sharma et al. (2016), the possibility of an inaccurate prescription of metallicity being responsible for the mismatch between observed and predicted mass distributions has not been investigated so far. Many studies have attempted to characterize the metallicity distribution of the thin and thick discs. For the thin disc, there is a well-defined radial metallicity gradient ($\approx -0.07$ dex kpc$^{-1}$; Robin et al. 2003; Hayden et al. 2014) but the age–metallicity relation is almost flat (Bensby, Feltzing & Oey 2014; Casagrande et al. 2016; Xiang et al. 2017; Silva Aguirre et al. 2018). For the thick disc, there is a lack of consensus regarding its properties. The Besançon model adopted a mean metallicity value of [Fe/H] $= -0.78$ based upon spectroscopic measurements by Gilmore, Wyse & Jones (1995) (mean thick disc [Fe/H] $\sim -0.6$) and photometric ($U$, $B$, $V$ bands) measurements by Robin et al. (1996). The *Galaxia* model (Sharma et al. 2011) used by Sharma et al. (2016, 2017) also adopted the same prescription for metallicity distribution of Galactic components as the Besançon model. However, at least four separate studies have compared predictions of the Besançon Galaxy model with that of spectroscopic observations and find that away from the mid-plane and in regions where the thick disc dominates, the metallicity distribution of the model is inconsistent with observations and that a shift of the thick disc metallicity from $-0.78$ to about $-0.48$ is required to make the model agree with observations. Specifically, Soubiran, Bienaymé & Siebert (2003) concluded the thick disc metallicity to be [Fe/H] $= -0.48 \pm 0.05$ by spectroscopically studying about 400 red clump stars in the direction of the North Galactic Pole at a height of $200 < z/{\rm pc} < 800$. Their spectra covered 390–680 nm at $R \sim 42\,000$. Kordopatis et al. (2011) reached their conclusions by studying a sample of about 700 F, G, and K dwarfs at a height $1 < z/{\rm kpc} < 4$ using the GIRAFFE spectrograph (820.6–940 nm at $R \sim 6500$). They suggested an overall metallicity of [M/H] $\sim -0.48$ for the thick disc. Note, the [M/H] of Kordopatis et al. (2011) is probably close to [Fe/H] but the exact relationship is not known. Boeche et al. (2013, 2014) used *Galaxia* to compare predictions of the Besançon model with stars from RAVE (841–879.5 nm at $R \sim 7500$) and found that for $|z| > 800$ pc, a better match to observations is obtained if [Fe/H] of the thick disc is set to $-0.5$. The former study makes use of dwarfs while the latter uses giants. More recently, results of Hayden et al. (2015) using giants from the APOGEE survey (1.51–1.70 μm at $R \sim 22\,500$) also suggest a higher metallicity ([Fe/H] $= -0.36$) for the thick disc, by considering stars between $1 < z/{\rm kpc} < 2$ and Galactocentric radius of $5 < R/{\rm kpc} < 7$ to be thick disc stars. The TRILEGAL Galactic model (Girardi et al. 2005) uses an effective metallicity of $Z = 0.008$ for the thick disc, which implicitly takes the $\alpha$ enhancement into account. This translates to [Fe/H] $\sim -0.5$ (assuming $Z_\odot = 0.0152$ and [$\alpha$/Fe] $= 0.24$), which compared to the Besançon model is more in line with recent spectroscopic measurements but is still lower than the APOGEE measurements.

We now have a large sample of stars with very precise metallicity measurements from spectroscopic surveys like the Galactic Archaeology for HERMES (GALAH De Silva et al. 2015), K2-HERMES (a GALAH-like survey dedicated to K2 follow-up, Wittenmyer et al. 2018), and Apache Point Observatory Galactic Evolution Experiment (APOGEE Majewski et al. 2017) surveys. In this paper, we use data from the GALAH survey to determine the metallicity distribution of the stellar populations in the Besançon-based Galactic model that we later use for asteroseismic analysis. Observationally, it is difficult to measure the metallicity of the stellar populations like the thin and the thick discs that are used in Galactic models. This is because the thick and thin discs overlap considerably such that it is difficult to identify individual stars belonging to each of the discs. Hence, we adopt a forward modeling approach where we fit a Galactic model to the observed data and try to answer the following question. What is the metallicity of the thick and thin discs that best describes the spectroscopic data from GALAH? Next, we use data from the APOGEE survey to verify our best-fitting model. Unlike spectroscopic studies of *Kepler* seismic targets, the photometric selection function of the K2-HERMES stars is almost the same as for the K2GAP seismic targets. (However, the angular area covered by K2-HERMES is typically smaller than that of the K2GAP). We take advantage of the selection function similarity to then directly check if the metallicity distribution of the K2GAP asteroseismic data, whose mass distributions we wish to compare with Galactic models, is in agreement with the models.

Finally, unlike the original *Kepler* survey, which was confined to one direction of the sky, the K2 targets span along the ecliptic allowing us to test our Galactic models in various regions of the Galaxy. Of particular importance is the ability of K2 to investigate the thick disc of the Milky Way. The thick disc is one of the most intriguing components of the Galaxy and its origin is not well understood. Compared to the thin disc, it is old, alpha-enhanced, metal poor, has higher velocity dispersion, and has a larger scale height. A complication with the thin disc versus thick disc nomenclature, is that the scale length for the thick disc is shorter than for the thin disc (Bovy et al. 2012; Mackereth et al. 2017; Xiang et al. 2017); the thick disc truncates near the solar circle where the thin disc dominates and beyond the solar circle the thin disc flares with increasing Galactic radius (see discussion and fig. 1 in Bland-Hawthorn et al. 2018). Although numerous spectroscopic surveys have targeted thick disc stars, a characterization of the thick disc using asteroseismic data has not been carried out. It was not possible to do using the *Kepler* data because its field of view was close to the Galactic plane. To move beyond this limitation, a number of K2GAP campaigns were selected at high Galactic latitudes, which means that a significant fraction of stars in the K2GAP are expected to be thick disc stars. Here, we use the K2 data to answer the following question. What is the thick disc age that best describes the seismic masses and spectroscopic data?

Downloaded from https://academic.oup.com/mnras/article/490/4/5335/5586605 by guest on 07 December 2020

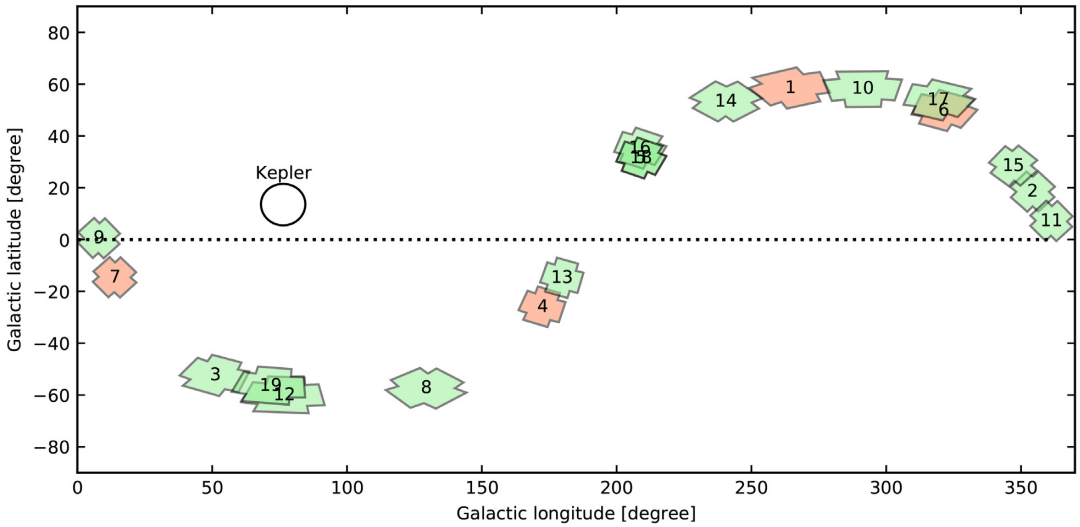


**Figure 1.** Field of view of K2 campaigns 1–19 in Galactic coordinates. Orange campaigns (C1, C4, C6, and C7) are studied in this paper. Campaigns C1 and C6 are at high Galactic latitude pointing away from the Galactic mid-plane, while campaigns C4 and C7 are at low Galactic latitude close to the Galactic plane. Campaign C7 is towards the Galactic center at (0, 0) and C4 is towards the Galactic anticentre.

The paper is structured as follows. In Section 2, we describe the asteroseismic and spectroscopic data used for the study. In Section 3, we discuss the methods that we use. Here we describe the selection function of the sample and discuss how we take it into account when forward modeling the simulated Galactic data. In Section 4, we present our results where we compare model predictions with observations and also tune the metallicity and the age distributions in our model to fit the data. In Section 5, we discuss and conclude our findings.

## 2 DATA

### 2.1 Asteroseismic data

The primary sample of stars in this study were observed by K2 as part of the K2GAP Guest Observer program (Stello et al. 2015, 2017). The stars that we use span four K2 campaigns − C1, C4, C6, and C7 − whose sky distributions are shown in Fig. 1. These K2 campaigns cover different regions of the Galaxy and sample a wide variety of Galactic stellar populations including old, young, thin disc, thick disc, inner disc, and outer disc. C1 and C6 are at high galactic latitudes and hence are likely to have more thick disc and old thin disc stars owing to the larger scale height of such stars. C4 and C7 are at lower latitudes and are likely to be dominated by young thin disc stars. C4 is towards the Galactic anticentre and samples the outer disc, whereas C7 is towards the Galactic centre and samples the inner disc.

The stars follow a simple colour magnitude selection based on the 2MASS photometry, which is given in Table 1. The following equation was used to convert 2MASS magnitude to an approximate *V*-band magnitude (Sharma et al. 2018).

$$V_{JK} = K + 2.0(J - K_s + 0.14) + 0.382\exp[(J - K - 0.2)/0.50] \quad (1)$$

Stars having good quality photometry from 2MASS were used; the exact criterion is shown in Table 2. Also listed are the criteria for the spectroscopic sample from the K2-HERMES survey, which for the 'Qflag' is slightly stricter than for the K2GAP targets. Only a subset of the K2GAP stars were observed by the K2-HERMES survey the number of which is also listed in Table 1. The K2-HERMES survey observes K2GAP stars that have magnitudes in range $10 < V_{JK} < 15.0$ and that lie in 1 deg radius circular fields. There are 19 such K2-HERMES fields for each K2 campaign and their layout for campaign C7 is shown in Fig. 2(d). In Table 1, *c* denotes the pointing identifier of these 1 deg radius fields.

In the K2GAP survey, the proposed stars were ranked in priority by *V* magnitude. For the dense campaign C7, they were additionally restricted to only three circular fields, to make the spectroscopic follow-up more efficient. During the final K2 mission-level target selection process for each campaign, the K2GAP target list was truncated at an arbitrary point (*V*-magnitude) based on target allocation. Hence, those selected stars will follow the K2GAP selection function. However, targets from other successful Guest Observer programmes that overlap with lower ranked (fainter) K2GAP targets could still end up being observed. These stars would not satisfy the K2GAP selection function. It is straightforward to locate the truncation point from the lists of proposed and observed targets by plotting the fraction of proposed to observed stars as a function of row number. A sharp fall in this ratio identifies the location of the truncation point. The K2GAP-proposed stars, the K2GAP-observed stars, and the K2GAP-observed stars following the K2GAP selection function are listed in Table 1.

The K2 time-series photometry is sampled roughly every 30 min, and span about 80 d per campaign. This allows us to measure the seismic signal in giants brighter than *Kepler* magnitude, *Kp*, of ∼15 in the range $10 \lesssim \nu_{\rm max}/\mu{\rm Hz} \lesssim 270$ ($1.9 \lesssim \log g \lesssim 3.2$), with a slight detection bias against the faint high $\log g$ stars due to their higher noise levels and lower oscillation amplitudes (Stello et al. 2017). We adopt the seismic results from the CAN pipeline (Kallinger et al. 2010), which is based on a Bayesian MCMC schemes and provides statistically robust uncertainties on each measurement. For C1 the seismic results were presented in Stello et al. (2017) while for C4, C6, and C7 they will be presented in Zinn et al. (in preparation). Throughout the paper we focus on stars with $10 < \nu_{\rm max}/\mu{\rm Hz} < 270$. A detailed description of the seismic analysis is given in Stello et al. (2017) and reference therein. The distribution

Downloaded from https://academic.oup.com/mnras/article/490/4/5335/5586605 by guest on 07 December 2020

**Table 1.** Number of K2 GAP targets for each campaign.

| Campaign | Proposed | Observed | Following selection | $N_{\rm giants}$ with $\nu_{\rm max}$ | $N_{\rm giants}$ with $\Delta\nu$ | $N_{\rm giants}$ $\nu_{\rm max}$ + spec. | Selection function |
|---|---|---|---|---|---|---|---|
| 1 | 9108 | 8630 | 8598 | 1104 | 583 | 455 | $((J-K_s)>0.5)\&(7<H<12.927)$ |
| 6 | 8371 | 8311 | 8301 | 1951 | 1452 | 504 | $((J-K_s)>0.5)\&(9<V_{JK}<15.0)$ |
| 4 | 17410 | 6357 | 4937 | 1839 | 945 | 702 | $((J-K_s)>0.5)\&(9<V_{JK}<13.447)$ |
| 7 | 8698 | 4361 | 4085 | 1541 | 1041 | 930 | $(J-K_s)>0.5)\&$ $((9<V_{JK}<14.5)\&(c\in\{6,17\})$ OR $((14.276<V_{JK}<14.5)\&(c\in\{14\}))$ |

*Note*. Circular pointing identifier $c$ is shown in Fig. 2(d).

**Table 2.** 2MASS quality selection criteria.

| fFlag | K2GAP criterion | K2-HERMES criterion | Description |
|---|---|---|---|
| Qflag | ≤'BBB' | ='AAA' | $J$, $H$, $K$ photometric quality |
| Bflag | ='111' | ='111' | Blend flag |
| Cflag | ='000' | ='000' | Contamination flag |
| Xflag | =0 | =0 | |
| Aflag | =0 | =0 | |
| prox | >6 arcsec | >6 arcsec | Distance to nearest star |

of K2GAP stars in the ($\log \nu_{\rm max}, J-Ks$) plane is shown in Fig. 3. In summary, automated analysis pipelines perform the measurements of the two seismic quantities used here: the frequency of maximum oscillation power, $\nu_{\rm max}$, and the frequency separation between overtone oscillation modes, $\Delta\nu$. Typically, only 50–70 per cent of stars for which oscillation are detected (meaning $\nu_{\rm max}$ is determined) do the pipelines also measure a robust $\Delta\nu$ (Stello et al. 2017).

In this paper, in addition to comparing the predictions of Galactic models against results from K2, we also compare against the results from the *Kepler* mission. For this we use the catalog of oscillating giants by Stello et al. (2013), in which the global seismic parameters were estimated using the Huber et al. (2009) pipeline (SYD). The exact selection function of oscillating giants in *Kepler* is not known. However, an approximate formula

$$3.731R_{\odot} < R_{\rm KIC} < \frac{3.7R_{\rm Earth}}{\sqrt{7.1\sigma_{\rm LC}/55.37}}, \quad (2)$$

was derived by Sharma et al. (2016) and we use this to sub-select targets from the above catalogue. Here, $R_{\rm KIC}$ is the photometry-based stellar radius as given in the *Kepler* input catalog of Brown et al. (2011),

$$\sigma_{\rm LC} = (1/c_{\rm Kepler})\sqrt{c_{\rm Kepler} + 7\times10^6 \max(1, Kp/14)^4} \quad (3)$$

is the long cadence (LC) noise to signal ratio, and $c_{\rm Kepler} = 3.46\times10^{0.4(12-Kp)+8}$ is the number of detected electrons per LC sample (Jenkins et al. 2010). For comparing the *Kepler* results with Galactic models, the synthetic $g$-band SDSS photometry was corrected using equation (4) from Sharma et al. (2016) and then $R_{\rm KIC}$ was estimated from synthetic photometry using the procedure outlined in Brown et al. (2011).

### 2.2 Spectroscopic data

The spectroscopic data come from the K2-HERMES (for seismic K2 targets) and the GALAH surveys (non-seismic targets) being conducted at the 3.9-m AAT located at Siding Spring observatory in Australia. The spectra were collected using the multi-object High Efficiency and Resolution Multi-Element Spectrograph (HERMES) spectrograph (Sheinis et al. 2015). The field of view of HERMES is a circular field of 1 deg radius. Each observed field has a unique field center and is tagged by a unique `field_id`. The K2-HERMES survey uses the same instrument set-up as the GALAH survey (Martell et al. 2017) and the TESS-HERMES survey (Sharma et al. 2018). The reduction is done using a custom IRAF-based pipeline (Kos et al. 2017). The spectroscopic analysis is done using the GALAH pipeline and is described in Buder et al. (2018). It uses Spectroscopy Made Easy (SME) to first build a training set by means of a model driven scheme (Piskunov & Valenti 2017). Next, *The Cannon* (Ness et al. 2015) is used to estimate the stellar parameters and abundances by means of a data driven scheme. To get Galactocentric cylindrical coordinates $R$ and $z$ for GALAH stars, we used parallaxes from *Gaia* DR2 (Gaia Collaboration 2016, 2018).

## 3 METHODS

### 3.1 Galactic models

In this paper we perform two kinds of analysis, one is to compare the predictions of theory with observations and the other is to fit Galactic models to the observed data. For this, we use population synthesis based Galactic models. The models consist of four different Galactic components, the thin disc, the thick disc, the bulge, and the stellar halo. The full distribution of stars in space, age, and metallicity $Z$, is given by

$$p(R,z,Z,\tau|\theta) = \sum_k p(k)p(R,z,Z,\tau|\theta,k), \quad (4)$$

with $k$ denoting a Galactic component, $\theta$ the parameters governing the Galactic model, $R$ the Galactocentric cylindrical radius, $z$ the height from the Galactic plane, $\tau$ the age, and $Z$ the metallicity of the stars in the Galactic component. To sample data from a prescribed population synthesis model we use the *Galaxia*[1] code (Sharma et al. 2011). It uses a Galactic model that is initially based on the *Besançon* model by Robin et al. (2003) but with some crucial modifications. The density laws and the initial mass functions for the various components are given in table 1 of Sharma et al. (2011) and are the same as in Robin et al. (2003). The density normalizations for various components are given in Table 3, these differ slightly from Robin et al. (2003) and a discussion of the changes is given in section 3.6 of Sharma et al. (2011). The thin disc spans an age range of 0–10 Gyr and has a star formation rate that is almost constant. The thin disc has a scale height that increases with age according to equation (18) in Sharma et al. (2011). In this paper, we leave the

[1] http://galaxia.sourceforge.net



Downloaded from https://academic.oup.com/mnras/article/490/4/5335/5586605 by guest on 07 December 2020

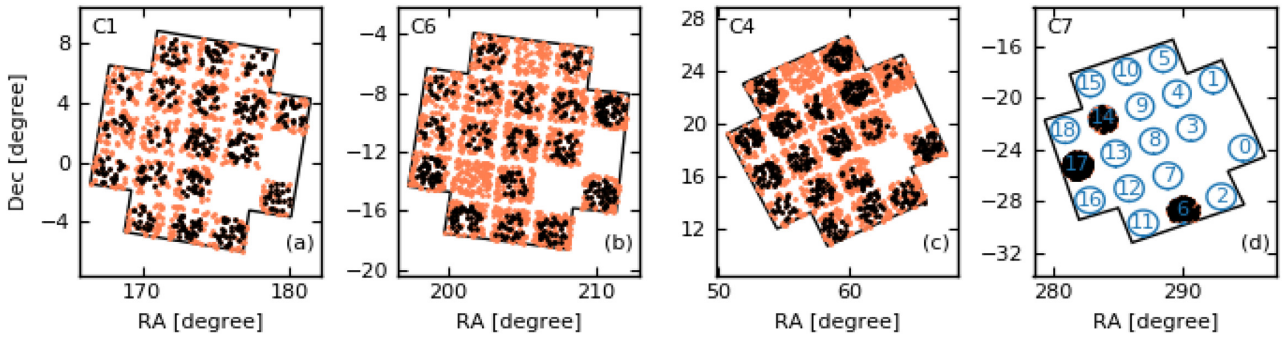


**Figure 2.** Angular distribution of the seismic sample on sky (orange dots). Each field of view comprises of 21 CCD modules with a small spacing between them. Two CCD modules were broken and hence no observations fall within them. Black dots are stars with spectroscopic information from the K2-HERMES survey. The black dots lie within a circle of 1 deg radius centred on the CCD modules. Campaigns C1, C4, and C6 have no angular selection for the seismic sample. In C7, stars are confined to three circular regions. Panel (d) shows the K2-HERMES sky pointings and their identifier.

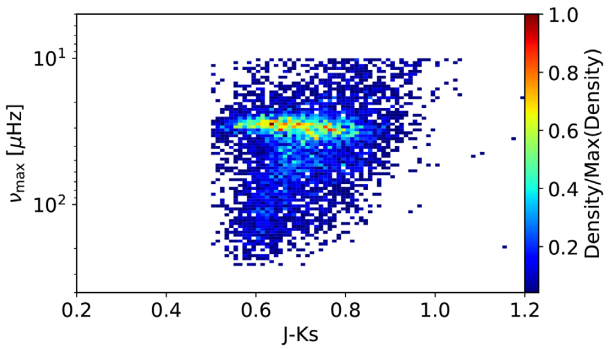


**Figure 3.** Distribution of K2GAP stars in the ($\log \nu_{max}$, $J - Ks$) plane, which resembles the ($\log g$, $T_{eff}$) plane. The overdensity at $\nu_{max} \sim 30$ μHz is due to RC stars. The sharp left edge in colour is due to the $J - Ks > 0.5$ selection function. The top and bottom edges are because $\nu_{max}$ can be reliably measured only in the range $10 < \nu_{max}/\mu\text{Hz} < 270$ with K2.

**Table 3.** The IMFs and the density normalizations of Galactic components. The parameters $\alpha_1$ and $\alpha_2$ are used to specify the IMF (number density of stars as a function of stellar mass, $M$), which is of the following form, $\propto M^{\alpha_1}$ for $M/\mathrm{M}_\odot < 1$ and $\propto M^{\alpha_2}$ for $M/\mathrm{M}_\odot > 1$.

| Galactic component | Normalization | $\alpha_1$ | $\alpha_2$ |
|---|---|---|---|
| Thin ($0 <$ Age/Gyr $< 7$) | 2.37 $\mathrm{M}_\odot\,\mathrm{yr}^{-1}$ [a] | −1.6 | −3.0 |
| Thin ($7 <$ Age/Gyr $< 10$) | 1.896 $\mathrm{M}_\odot\,\mathrm{yr}^{-1}$ [a] | −1.6 | −3.0 |
| Thick | $\rho_{\odot,\mathrm{thick}}$ [b] | −0.5 | −0.5 |
| Stellar halo | $10.252 \times 10^3 \mathrm{M}_\odot\,\mathrm{pc}^{-3}$ [b] | −0.5 | −0.5 |
| Bulge | 13.76 stars $\mathrm{pc}^{-3}$ [c] | −2.35 | −2.35 |

*Notes.* [a]Star formation rate for an IMF spanning a mass range of 0.07–100 $\mathrm{M}_\odot$.
[b]Local mass density of visible stars.
[c]Central density.

thick disc normalization as a free parameter and solve for it using data from *Gaia* DR2.

Other differences between *Galaxia* and the *Besançon* model are as follows. *Galaxia* is a robust statistical sampler, it provides continuous sampling over any arbitrary volume of the Galaxy. This enables rigorous comparisons with observed stellar surveys for an arbitrary selection function. *Galaxia* has a 3D extinction scheme that is based on Schlegel, Finkbeiner & Davis (1998) dust maps. We also apply a low-latitude correction to the dust maps as

**Table 4.** Galactic models with different age and metallicity distribution functions.

| Model | | Thick | Thin[a] |
|---|---|---|---|
| MP[b] | ⟨[M/H]⟩ | −0.78 | [0.01, 0.03, 0.03, 0.01, −0.07, −0.14, −0.37] |
| | $\sigma_{[M/H]}$ | 0.33 | [0.12, 0.12, 0.10, 0.11, 0.18, 0.17, 0.2] |
| | Min(Age[c]) | 11 | [0, 0.15, 1, 2, 3, 5, 7] |
| | Max(Age) | 11 | [0.15, 1, 2, 3, 5, 7, 10] |
| MR | ⟨[M/H]⟩ | −0.162 | [0.01, 0.03, 0.03, 0.01, 0, 0, 0] |
| | $\sigma_{[M/H]}$ | 0.17 | Same as MP |
| | Min(Age) | 9 | Same as MP |
| | Max(Age) | 11 | Same as MP |
| FL | ⟨[M/H]⟩ | −0.14 | 0.0 |
| | $\sigma_{[M/H]}$ | 0.30 | 0.3 |
| | Min(Age) | 6 | Same as MP |
| | Max(Age) | 13 | Same as MP |

*Notes.* [a]Thin disc consists of seven distinct populations with different age ranges and $\mathrm{d[M/H]/d}R = -0.07\ \mathrm{dex\,kpc}^{-1}$.
[b]The [M/H] values correspond to [Fe/H] values used by Robin et al. (2003), ignoring $\alpha$ enhancement.
[c]In units of Gyr.

described in Sharma et al. (2014). The isochrones used to predict the stellar properties are from the Padova database using CMD 3.0 (http://stev.oapd.inaf.it/cmd), with PARSEC-v1.2S isochrones (Bressan et al. 2012; Chen et al. 2014, 2015; Tang et al. 2014), the NBC version of bolometric corrections (Chen et al. 2014), and assuming Reimers mass-loss with efficiency $\eta = 0.2$ for RGB stars. The isochrones are computed for scaled-solar composition following the $Y = 0.2485 + 1.78Z$ relation and their solar metal content is $Z_\odot = 0.0152$.

The details of the different Galactic models that we use in this paper are given in Table 4. The base *Galaxia* model denoted by MP (metal poor) is from Sharma et al. (2011), it has an old metal poor thick disc and a thin disc whose mean metallicity decreases with age as in Robin et al. (2003). The model denoted by MR (metal rich) has metal rich thick and thin discs. The FL (flat) model also has a metal rich thick and thin disc, but unlike other models its thick disc spans an age range from 6 to 13 Gyr with a uniform star formation rate and no variation of metallicity with age. For each Galactic component $k$, the IMF, the formula for spatial distribution of stars, and the density normalizations are given in Sharma et al. (2011).

Downloaded from https://academic.oup.com/mnras/article/490/4/5335/5586605 by guest on 07 December 2020

To compare predictions of Galactic models to asteroseismic data, we need to estimate the observed seismic quantities $\nu_{\rm max}$ and $\Delta\nu$ for the synthetic stars. The seismic quantities are estimated from effective temperature, $T_{\rm eff}$, surface gravity, $g$, and density, $\rho$, using the following asteroseismic scaling relations (Ulrich 1986; Brown et al. 1991; Kjeldsen & Bedding 1995).

$$\frac{\nu_{\rm max}}{\nu_{\rm max,\odot}} = \frac{g}{g_\odot}\left(\frac{T_{\rm eff}}{T_{\rm eff,\odot}}\right)^{-0.5} \text{ and } \frac{\Delta\nu}{\Delta\nu_\odot} = f_{\Delta\nu}\left(\frac{\rho}{\rho_\odot}\right)^{0.5}. \quad (5)$$

Here,

$$f_{\Delta\nu} = \left(\frac{\Delta\nu}{135.1\ \mu{\rm Hz}}\right)\left(\frac{\rho}{\rho_\odot}\right)^{-0.5} \quad (6)$$

is the correction factor derived by Sharma et al. (2016) by analysing theoretical oscillation frequencies with GYRE (Townsend & Teitler 2013) for stellar models generated with MESA (Paxton et al. 2011, 2013). We used the code ASFGRID[2] (Sharma et al. 2016) that computes the correction factor as a function of metallicity $Z$, initial mass $M$, evolutionary state $E_{\rm state}$ (pre or post helium ignition), $T_{\rm eff}$, and $g$.

### 3.2 Selection function matched mock catalogues

In this paper we frequently compare the observed data with predictions from Galactic models. and additionally, we also fit models to the data. In order to do the comparison or fitting, we have to properly forward-model the simulated data and make it satisfy the same observational constraints that the observed data satisfies. The two main things to take into account are the foot print on the sky and the photometric selection criteria. The basic procedure is to select stars according to the selection function and then bin them up in the space of some observables and ensure that the number of stars in the mock catalogue match the number in the observed catalogue in each bin. Details of the procedure for the different surveys that we analyse in this paper is given below.

(i) K2GAP: We select stars according to the selection function of each campaign (eighth column of Table 1) and bin them up by campaigns. The number of observed stars satisfying the selection function is given in fourth column of Table 1.

(ii) K2GAP with K2-HERMES data: We select stars with the K2GAP selection function and with $10 < V(J, K) < 14.5$ and bin them up in (`field_id`, $V(J, K)$) space with bins of size 1 and 0.5.

(iii) *Kepler*: We select stars satisfying equation (2), $8 < Kp < 14$ and $0 < \log g_{\rm phot} < 6$ and then bin them up in ($Kp$, $\log g_{\rm phot}$) space with bin sizes of 0.3 and 0.25. Here, $g_{\rm phot}$ is surface gravity estimated from photometry.

(iv) GALAH: We select stars with $9 < V(J, K) < 14$ and bin them up in (`field_id`, $V(J, K)$) space with bins of size 1 and 0.5.

(v) APOGEE: We select stars with $9 < H < 14$, $0.5 < J - Ks < 2.5$, and $-5.2 < M_{Ks} < 1.8$ and bin them up in (`field_id`, $H$, $J - Ks$, $M_{Ks}$) space with bins of size 1, 0.25, 0.2, and 0.25.

The procedure above generates a base mock catalogue, additional selections based on other observables are applied to the base catalogue as needed, e.g. for the seismic samples selections of $10 < \nu_{\rm max}/\mu{\rm Hz} < 270$ (see Section 2.1) and $p_{\rm detect} > 0.9$ (see Section 3.4) are applied.

[2]http://www.physics.usyd.edu.au/k2gap/Asfgrid

### 3.3 Importance-sampling framework

To constrain the parameters of a Galactic model from the observed data we developed and used an importance-sampling framework, which we now describe. Suppose we have collected some data regarding some variable $x$, such as metallicity $Z$ or seismic mass, subject to some selection function $S$. Then suppose that we have a Galactic model parametrized by $\theta$ from which we can draw samples subject to the same selection function $S$. To constrain the model, we start with a base model parametrized by some $\theta_0$, then to change the model into one parametrized by a new $\theta$, we simply reweight the samples from the simulation parametrized by $\theta_0$ instead of drawing from a new simulation. When the model changes from $\theta_0$ to $\theta$, the new weights for a star $i$ belonging to a Galactic component $k$ are given by

$$w_i = p(R_i, z_i, Z_i, \tau_i|\theta, k)/p(R_i, z_i, Z_i, \tau_i|\theta_0, k). \quad (7)$$

In general, such a change can alter the number of visible stars of your synthetic Galaxy, but as long as the parameters governing the density distribution of the stars are unaltered, the changes are minimal. In this paper, we are mainly concerned with only altering the thick disc parameters like mean age and metallicity. We also alter the metallicity of the old thin disc, but this change is minor and can be ignored for the present discussion related to the number of visible stars. The base model that we use is based on the Besançon model, which was constructed by Robin et al. (2003) to satisfy the observed star counts in the Galaxy. When the thick disc parameters, like mean age and/or the metallicity are modified, we adopt the following procedure to address the slight change that is expected in the number of visible thick disc stars. We measure $f_{\rm SGP}$, the ratio of stars that lie between $2 < |z|/{\rm kpc} < 3$ out of all stars that are in a 30° radius cone around the south Galactic pole ($b = -90.0°$) and have *Gaia* magnitudes $0 < G < 14$ from *Gaia* DR2 (Gaia Collaboration 2018). Using $f_{\rm SGP}$ estimated from *Gaia* DR2, we solve for the normalization factor $\rho_{\odot,\rm thick}$ and reweight the thick disc of the model such that $f_{\rm SGP}$ in the selection-function-matched mock sample matches with that of the *Gaia* DR2 data. Following this global normalization, the stars are further re-weighted to satisfy the colour magnitude selection and survey footprint on the sky of the observational data to which the model is being fitted.

To fit the model to the data we need to compute the likelihood of the data given the model and this is done as follows. Let $x_q$ be the $q_{\rm th}$ percentile of the distribution of some variable $x$. For this variable, suppose we have observed samples $X_o$ and samples from some model $X_m$, with the model being parametrized by $\theta$ and $S$ being the selection function. The probability of the observed data given the model can then be written as

$$p(X_o|\theta, S) = \prod_q \frac{1}{\sqrt{2\pi}\sigma_x}\exp\left(-\frac{(x_{o,q} - x_{m,q})^2}{2\sigma_x^2}\right), \text{ with}$$
$$\sigma_x^2 = (\sigma_{x,\rm o}^2/n_{\rm eff,o} + \sigma_{x,\rm m}^2/n_{\rm eff,m}). \quad (8)$$

Here, $n_{\rm eff}$ is the effective number of stars, which for stars with different weights is given by $\left(\sum w_i\right)^2/\sum w_i^2$ according to Kish's formula. We make use of 16, 50, and 84 percentiles to compute the likelihood of the data given the model. The $x_{o,q}$ and $x_{m,q}$ denote the $q_{\rm th}$ percentile obtained from samples $X_o$ and $X_m$, respectively. For multiple data sets, $X = \{X_o^1, ..., X_o^{ns}\}$ with each of them having their own selection function $S' = \{S_1', ..., S_{ns}'\}$, the full likelihood is

$$p(X|\theta, S', S) = \prod_i p(X_o^i|\theta, S_i, S). \quad (9)$$

Downloaded from https://academic.oup.com/mnras/article/490/4/5335/5586605 by guest on 07 December 2020

Note, $S$ here is the global selection function, e.g. photometric and field selection, and $S'$ represents the selection function for additional partitioning of the data set, e.g. partitioning by bins in $R$ and $z$.

In this paper, the importance-sampling framework is used for estimating the metallicity of the thick disc using spectroscopic data from the GALAH survey and to estimate the age of the thick disc from the asteroseismic data from K2. For the former (metallicity estimation), we partition the data (selection $S'$) by binning up the stars lying in $5 < R/\mathrm{kpc} < 11$ and $1 < |z|/\mathrm{kpc} < 3$ using bins of size 0.5 kpc in $R$ and 0.33 kpc in $|z|$. We use $\log Z/Z_\odot$ as the observed variable $x$ and fit for the mean and the dispersion of the thick disc metallicity and the mean metallicity of the old thin disc (age greater than 3 Gyr) in the Galactic model. For this we use the MR model from Table 4. The global selection function $S$ in this case is given by $9 < V_{JK} < 14$, $0 \leq \texttt{field_id} < 7117$ and positive rotation about the Galaxy.

For the latter (age estimation), we partition the data (selection $S'$) by binning up the stars into different K2 campaigns and three different giant classes. We follow Sharma et al. (2016) by using the temperature-independent seismic mass proxy

$$\kappa_M = \left(\frac{\nu_{\max}}{\nu_{\max,\odot}}\right)^3 \left(\frac{\Delta\nu}{\Delta\nu_\odot}\right)^{-4} \tag{10}$$

as the variable $x$ and fit for the age (mean) and metallicity (mean and dispersion) of the thick disc. For this we use the FL model from Table 4. For each selection of stars the likelihood is computed using equation (8). The $\kappa_M$ is closely related to the stellar mass $M$, which is given by

$$\frac{M}{\mathrm{M}_\odot} = \kappa_M \left(\frac{T_{\rm eff}}{T_{\rm eff,\odot}}\right)^{1.5}. \tag{11}$$

Given that temperatures are not always readily available for the observed stars, we use $\kappa_M$ instead of mass when comparing theoretical predictions to observations. This also removes any ambiguity in temperature scale differences between the models and the data. For simplicity we will in the following refer to $\kappa_M$ as mass. The global selection function $S$ for this analysis is described in Section 2.1 and additionally we restrict to stars with $10 < \nu_{\max}/\mu\mathrm{Hz} < 270$ and $p_{\rm detect} > 0.9$ as described in the following section.

### 3.4 Detection completeness

Before we can compare the mass distributions or fit models, we also have to take seismic detection bias into account as part of the selection function.

The duration of the K2 campaigns sets a lower limit on the detectable $\nu_{\max}$ of about 10 μHz below which the seismic detection efficiency drops. The observational cadence sets an upper limit of about $\nu_{\max} = 270\,\mu$Hz (Stello et al. 2015). The amplitude of oscillations decreases with increasing $\nu_{\max}$ (less luminous stars) and the photometric noise increases towards fainter stars. This makes it harder to detect oscillations for stars that have higher $\nu_{\max}$ and/or are faint. This bias is clearly visible as missing stars in the top right corner of Fig. 4(a), (c), (e), and (g), which shows the distribution of observed stars in the ($\nu_{\max}$, $V_{JK}$) plane.

To model the seismic detection probability we followed the scheme presented by Chaplin et al. (2011a) and Campante et al. (2016). For this, we used the mass, radius, and effective temperature of each synthetic star to predict its total mean oscillation power and granulation noise in the power spectrum. The oscillation amplitude was estimated as $A = 2.5(L/L_\odot)^{0.9}(M/M_\odot)^{-1.7}(T_{\rm eff}/T_{\rm eff,\odot})^{-2}$ following Stello et al. (2011). The granulation power was estimated

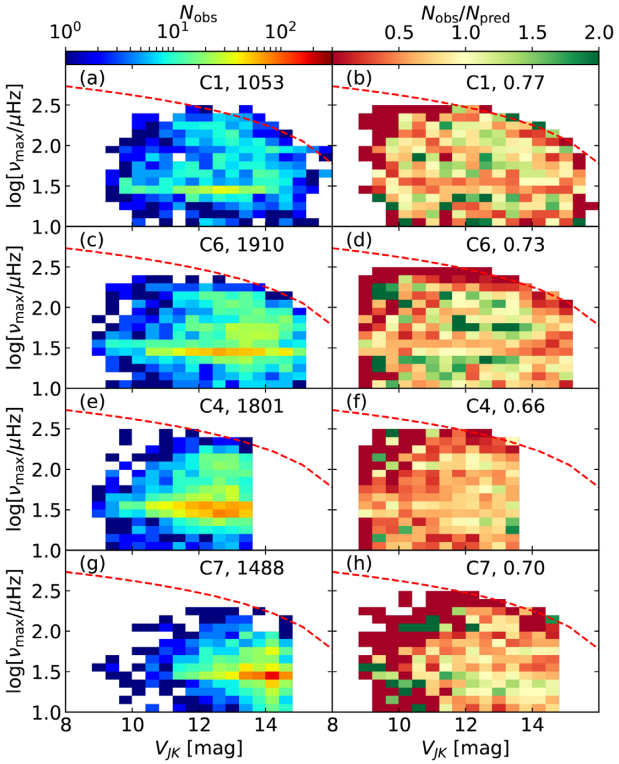


**Figure 4.** Distribution of observed (left-hand panels) stars in the ($\nu_{\max}$, $V_{JK}$) plane for four K2 campaigns. The right-hand panels plot the ratio of observed to predicted oscillating giants in each bin. The predictions are based on simulations using *Galaxia*. The dashed line represents the equation $\nu_{\max} = -60(V_{JK} - 17)$. The upper right region (above the dashed line) indicates where we cannot detect oscillations due to too low signal-to-noise.

using the Kallinger et al. (2014) model. The apparent magnitude was used to compute the instrumental photon-limited noise in the power spectrum, which combined with granulation noise gave the total noise. For the instrumental noise we use equation (3) (formula given by Jenkins et al. 2010). For K2, we scaled the noise by a factor of three to take into account the higher noise in the K2 data compared to the *Kepler* data and also applied a minimum threshold of 80 ppm. The mean oscillation power and the total noise were then used to derive the probability of detecting oscillations, $p_{\rm detect}$, with less than 1 per cent possibility of false alarm. Stars with $p_{\rm detect} > 0.9$ were assumed to be detectable.

The results of applying the detection probability on the *Galaxia* simulated stars are shown in Fig. 4(b), (d), (f), (h) as the ratio between the number of observed to predicted stars. The $\nu_{\max}$ was estimated using equation (5). The figure shows that the fraction of predicted to observed stars is close to one over most of the regions where we have observed stars. However, C4, C6, and C7 show a slight tendency of having a lower than predicted number of stars towards the top right corner of each panel (higher $V_{JK}$ and higher $\nu_{\max}$), where the signal-to-noise ratio of the oscillations is low. This is probably because for these campaigns, the detections are based solely on automated pipelines, with no additional visual inspection as for C1 (Stello et al. 2017). The mean detection fraction is 0.72, and the cause for fewer detections is not clear. Using the deep-learning-based pipeline of Hon, Stello & Yu (2018) resulted in slightly more $\nu_{\max}$ detections, raising the mean detection fraction to 0.78, but the fraction still remained significantly less than one.

Downloaded from https://academic.oup.com/mnras/article/490/4/5335/5586605 by guest on 07 December 2020

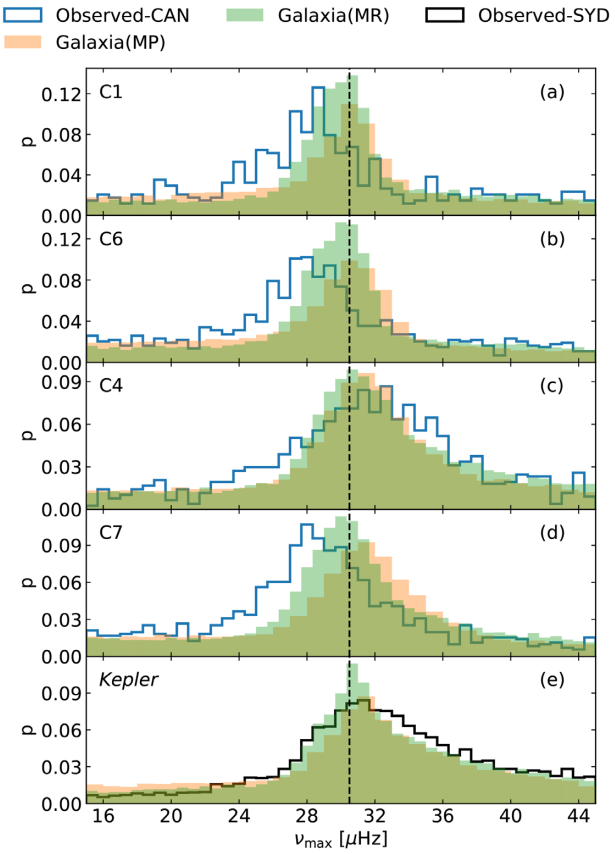


**Figure 5.** The probability distribution of $\nu_{max}$ for observed and predicted oscillating giants. The dashed line, $\nu_{max} = 30.5$ μHz, shows the approximate location of the peak in the distribution of the predicted stars. The peak corresponds to the location of the red clump giants. The location of the peak is not sensitive to the choice of the Galactic model, but the distribution is sharper for the MR model. The peak for the CAN pipeline is systematically lower as compared to the predictions, except for C4.

### 3.5 The distribution of $\nu_{max}$ and apparent magnitude

We now check the distribution of apparent magnitudes and $\nu_{max}$ in more detail. In Fig. 5, the $\nu_{max}$ distributions show a peak, which corresponds to the red clump stars. For the simulated data (orange line) the peak is close to 30.5 μHz [*Galaxia*(MR)]. The location of the peak varies very little across different campaigns, it is about 1 μHz higher for the low-latitude campaign C4 and *Kepler*. For all campaigns, the location of the peak for the CAN pipeline is systematically lower by 2 μHz compared to the predictions. The peak for the *Kepler* data obtained using the SYD pipeline does not show any shift with respect to the predicted peak. To conclude, we see some systematic differences between observations and predictions related to the location of the peak, they are small but could be important for certain applications and hence should be investigated further in future.

The corresponding distributions of $V_{JK}$ for K2 are shown in Fig. 6. Overall the observed distributions match well with the model predictions. For C6, the model predicts more stars for $V_{JK} > 13.5$, the cause of which is not yet clear, but we found that this has no impact on our conclusions related to the mass distribution of stars that we present in this paper.

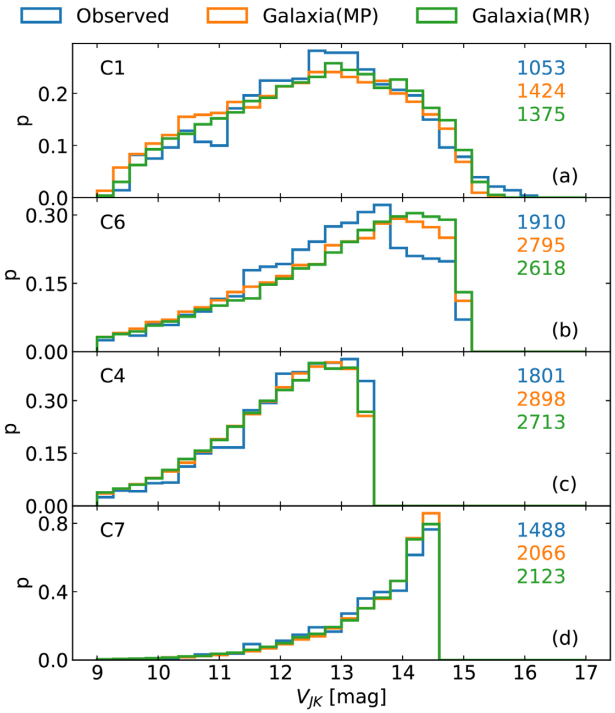


**Figure 6.** Magnitude distribution of observed oscillating giants from K2 along with predictions from *Galaxia* corresponding to model MP and MR. The number of stars with $\nu_{max}$ detections in the observed sample and those predicted by model MP, and MR are also listed in each panel.

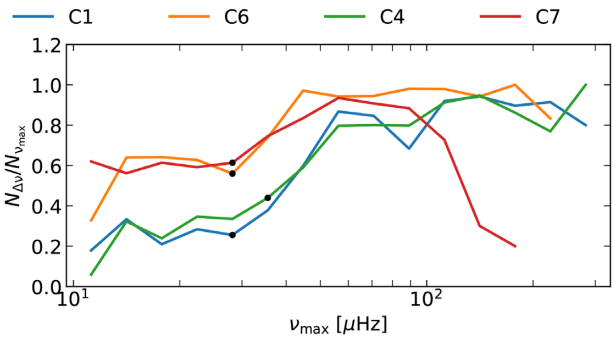


**Figure 7.** The ratio of the number of stars with and without $\Delta\nu$ measurements for various K2 campaigns. The black dot marks the frequency of the peak, $\nu_{max,RC}$, in the $\nu_{max}$ distribution of the observed stars and is due to RC stars. The ratio shows a sharp increase for stars with $\nu_{max} > \nu_{max,RC}$.

### 3.6 Classifying giants into different classes

In the seismic analysis, $\nu_{max}$ is easier to detect compared to $\Delta\nu$. Hence, there are stars with a $\nu_{max}$ measurement but no $\Delta\nu$ measurement and this needs to be taken into account when comparing model predictions with observations. To accomplish this, we first study the $\Delta\nu$-detection completeness of our sample and then devise ways to account for it when comparing model predictions with observations.

The probability, $p_{\Delta\nu}$, of having a $\Delta\nu$ measurement given that we have a measurement of $\nu_{max}$ is shown in Fig. 7, as a function of $\nu_{max}$. This was derived by binning the stars in $\nu_{max}$ and then computing in each bin the ratio of the number of stars with a $\Delta\nu$ measurement ($N_{\Delta\nu}$) to those with a $\nu_{max}$ measurement ($N_{\nu_{max}}$). We see three distinct phases. The first is for $\nu_{max} < 25$ μHz, where $p_{\Delta\nu}$ is constant but low. The second is for $25 < \nu_{max} < 50$ μHz, where $p_{\Delta\nu}$



Downloaded from https://academic.oup.com/mnras/article/490/4/5335/5586605 by guest on 07 December 2020

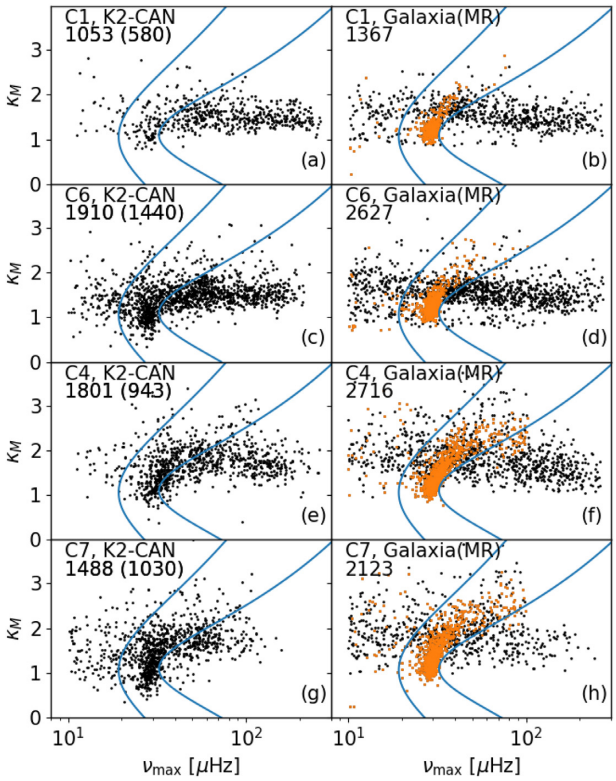


**Figure 8.** Distribution of stars in the ($\kappa_M$, $\nu_{max}$) plane. The blue lines split the plane into three distinct regions, the predominantly high-luminous RGB stars (left), the predominantly red-clump stars (middle), and the low-luminosity RGB stars (right). Left-hand panels (a, c, e, g) show results from K2 based on the CAN pipeline. Right-hand panels (b,d,f,h) show predictions from *Galaxia*. The overplotted orange points denote the red clump stars.

increases with $\nu_{max}$. And the third is for $\nu_{max} > 50\,\mu$Hz, where $p_{\Delta\nu}$ is again constant and close to 1 (except for C7 where $p_{\Delta\nu}$ is lower for $\nu_{max} > 100\,\mu$Hz). The drop in $p_{\Delta\nu}$ as $\nu_{max}$ decreases from 50 to 30 $\mu$Hz, coincides with the increase in fraction of red-clump stars as predicted by a *Galaxia* simulation (see orange dots in Fig. 8). This drop could be because the power spectra of red-clump stars are more complex than RGB stars (Chaplin & Miglio 2013) and this makes the $\Delta\nu$ measurement harder to obtain. For $\nu_{max} < 25\,\mu$Hz, we mainly have RGB stars, but the $p_{\Delta\nu}$ is still low, and this could be due to the limited frequency resolution of the K2 data starting to affect our ability to obtain a clear $\Delta\nu$ measurement towards the low $\nu_{max}$ stars. Although all four campaigns show similar $p_{\Delta\nu}$ for high $\nu_{max}$ stars, we note that for $\nu_{max} < 30\,\mu$Hz, $p_{\Delta\nu}$ is about a factor of two lower for C1 and C4 compared to C6 and C7. The cause for this different behaviour is not clear.

We have seen in Fig. 7 that $\Delta\nu$ detections are incomplete with a completeness that depends on $\nu_{max}$, which being proportional to surface gravity is closely linked to stellar type (evolution stage). This suggests that we should study the different types of giants separately. Below we describe a scheme to segregate stars into three giant classes: the high-luminosity RGB stars, the RC stars, and the low-luminosity RGB stars. The segregation is done in the ($\kappa_M$, $\nu_{max}$) plane. By construction, the high-luminosity RGB class will have some contamination from AGB stars and the RC class will have contamination from RGB stars.

Fig. 8 shows the distribution of stars in the ($\kappa_M$, $\nu_{max}$) plane both for the observed and *Galaxia*-simulated data. Although RC stars typically have $\nu_{max} \sim 30\,\mu$Hz, Fig. 8 shows that the high $\kappa_M$ stars can have $\nu_{max}$ reaching up to $\sim$100 $\mu$Hz. This is the main reason why we decided not to isolate RGB stars solely from their $\nu_{max}$. Based on simulations by *Galaxia*, we instead fit and obtain two curves

$$\nu_{max}^{lower} = 6.8478\,\kappa_M^2 - 14.489\,\kappa_M + 26.914 \quad (12)$$

$$\nu_{max}^{upper} = 33.598\,\kappa_M^2 - 73.523\,\kappa_M + 72.647 \quad (13)$$

that enclose about 92 per cent of the RC stars (blue lines). In Fig. 8, it can be seen that the red clump stars are nicely enclosed by the blue lines.

These curves are then used to classify stars into the three categories: (a) $\nu_{max} < \nu_{max}^{lower}$ (high-luminosity RGB stars or hRGB), (b) $\nu_{max}^{lower} < \nu_{max} < \nu_{max}^{upper}$) (RC stars), and c) $\nu_{max} > \nu_{max}^{upper}$ (low-luminosity RGB stars or lRGB). Based on *Galaxia* simulations, the fraction of RGB stars in the three categories averaged across all campaigns was found to be (a) 0.87, (b) 0.18, and (c) 0.97, suggesting that each category is dominated by the desired stellar type in that category, i.e. RGB, RC, and RGB, respectively.

## 4 RESULTS

### 4.1 Constraints from spectroscopic surveys

Large-scale surveys of the Milky Way were not available at the time the *Besançon* model was constructed as implemented in *Galaxia*. The situation has changed now, with surveys like APOGEE and GALAH providing high-resolution spectra for hundreds of thousands of stars, which sample the Galaxy well beyond the solar neighborhood. Hence it is possible to characterize the thick disc better than before.

To study the elemental composition of the thick disc we need to identify stars belonging to the thick disc. This can be done using height above the Galactic plane or rotational velocity. We choose the former approach as the overlap of the thin and thick disc is quite strong in rotational velocity. To isolate thick disc stars, we select stars with ($5 < R/\mathrm{kpc} < 7$) and $1 < |z|/\mathrm{kpc} < 2$. This region provides the largest number of thick disc stars with the least amount of contamination from the thin disc, as can be seen in fig. 4 from Hayden et al. (2015). In Fig. 9, we further illustrate this using data from the GALAH survey Buder et al. (2018). There are hints of three populations in Fig. 9(a); the thin disc at [Fe/H] $\sim 0$, the thick disc at [Fe/H] $\sim -0.39$, and the stellar halo at [Fe/H] $\sim -1.75$. After selecting stars by location, the thin disc sequence almost vanishes and the halo can be seen as a weak overdensity in Fig. 9(b). For this particular spatial selection, the median and the spread of the distribution of [Fe/H] and [$\alpha$/Fe] are listed in Table 5 and compared with that of APOGEE-DR14. Also given are metallicity estimates [M/H] constructed using the formula

$$[\mathrm{M/H}] = \log\left(\frac{Z}{Z_\odot}\right) = [\mathrm{Fe/H}] + \log(10^{[\alpha/\mathrm{Fe}]}0.694 + 0.306). \quad (14)$$

by Salaris & Cassisi (2005). Given an isochrone grid constructed for metallicities $Z$ using solar-scaled composition with a specified $Z_\odot$, the above formula provides an approximate estimate of metallicity $Z$ or [M/H] for a given [Fe/H] and [$\alpha$/Fe]. In Table 5 we choose to show the median, however, we also compared them with the mean values. Their differences was less than 0.01 dex (after discarding stars with [Fe/H] $<-1.25$, which most likely belong to the stellar halo).

Downloaded from https://academic.oup.com/mnras/article/490/4/5335/5586605 by guest on 07 December 2020

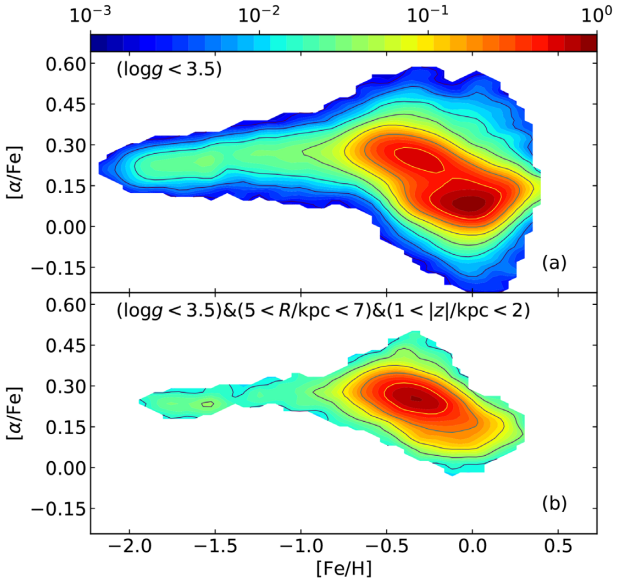


**Figure 9.** Distribution of GALAH giants in the ([Fe/H], [α/Fe]) plane. Giants were selected using $\log g < 3.5$. (a) Distribution of all giants. (b) Giants restricted to $5 < R/\mathrm{kpc} < 7$ and $1 < |z|/\mathrm{kpc} < 2$. The colour bar shows probability density, which is normalized such that the maximum density is 1.

**Table 5.** Abundance of iron and alpha elements for thick disc stars. The first four rows show the median and standard deviation based on 16th and and 84th percentile values for stars with $5 < R/\mathrm{kpc} < 7$ and $1 < |z|/\mathrm{kpc} < 2$ and positive rotation about the Galaxy. The last row shows the result obtained by fitting a Galactic model.

| Source | [Fe/H] | | [α/Fe] | | $\log(Z/Z_\odot)$ | |
|---|---|---|---|---|---|---|
| | med | sdev | med | sdev | med | sdev |
| APOGEE-DR14 | −0.294 | 0.28 | 0.186 | 0.08 | −0.160 | 0.24 |
| GALAH DR2 | −0.367 | 0.24 | 0.218 | 0.08 | −0.196 | 0.21 |
| GALAH DR2c[a] | −0.316 | 0.21 | 0.239 | 0.07 | −0.131 | 0.18 |
| GALAH mock[b] | | | | | −0.170 | 0.25 |
| GALAH DR2c[c] | | | | | −0.16 | 0.17 |

*Notes.* [a]Calibrated.
[b]Mock GALAH catalogue generated by *Galaxia* with $\log(Z/Z_\odot) \sim \mathcal{N}(-0.18, 0.22^2)$ for the thick disc.
[c]Fitting a Galactic model to GALAH stars with $5 < R/\mathrm{kpc} < 11$, $0.75 < |z|/\mathrm{kpc} < 3$, $9 < V_{JK} < 14$, $0 \leq$ `field_id` $< 7117$ and positive rotation about the Galaxy.

In Table 5, two different estimates are given for GALAH, the first is based on the GALAH DR2 pipeline, the second named GALAH DR2c is based on a calibration correction that we derive and apply to the GALAH DR2 estimates. GALAH DR2 estimates are based on *The Cannon* method (Ness et al. 2015), which was trained on results from the SME (Piskunov & Valenti 2017) pipeline. However, as shown in Fig. 10, for giants we find subtle systematics in the GALAH DR2 stellar parameters compared to that of SME estimates, where $\nu_{\max}$ estimated from asteroseismology was used as a prior. The systematics are particularly significant for stars with [Fe/H] > 0.0. We use the seismic giants in the SME training set to recalibrate the GALAH results. The coefficients of the calibration equation are given in Table 6. A comparison of GALAH stellar parameters (both calibrated and uncalibrated) with those from APOGEE for common stars is shown in Fig. 11. It is the calibrated GALAH gravities and temperatures that match best with APOGEE. In the range −0.5 < [Fe/H] < 0.0, where the majority of the sample is found, the calibrated [Fe/H] also matches better with APOGEE. Outside this range some systematics exist. The [α/Fe] shows slight offsets in zero-points but no significant trend is seen.

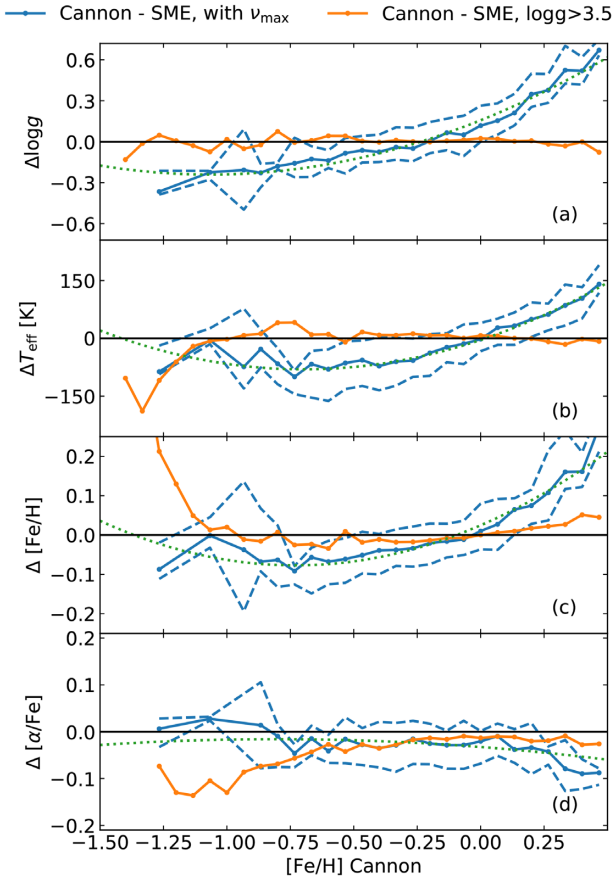


**Figure 10.** Comparison of GALAH-DR2 Cannon-based (data-driven) estimates to that of SME-based (model-driven) estimates. The plots show systematic trends as a function of Cannon-based iron abundance [Fe/H]. The giants (blue) and dwarfs (orange) are shown separately. The giants shown are seismic giants from K2, and for them SME was run using $\nu_{\max}$ estimated from asteroseismology as a prior. The seismic giants show strong systematic trends while dwarfs have negligible systematics. The dotted line is a two degree polynomial fit to the trends for the seismic giants with $-1.5 <$ [Fe/H] $< 0.3$.

**Table 6.** Polynomial coefficients of calibration equation $y_{\rm calib} = y + c_0 + c_1[\mathrm{Fe/H}] + c_2[\mathrm{Fe/H}]^2$ to correct for systematics in the Cannon-based estimates against the SME-based estimates. The equation was derived using giants having $\nu_{\max}$ estimates from asteroseismology and with $-1.5 <$ [Fe/H] $< 0.3$. The calibration is applied to giants with [Fe/H] $> -1.5$, the giants are identified using the Ciardi et al. (2011) definition.

| $y$ | $c_2$ | $c_1$ | $c_0$ |
|---|---|---|---|
| $\log g$ | +3.4987e−01 | +7.4591e−01 | +1.5727e−01 |
| $T_{\rm eff}$ K | +1.5658e+02 | +2.1861e+02 | −3.9895e+00 |
| [Fe/H] | +1.9087e−01 | +2.7875e−01 | +2.4761e−02 |
| [α/Fe] | −2.5775e−02 | −4.1510e−02 | −3.2592e−02 |

We see from Table 5 that the estimates for the mean metallicity of stars above the mid-plane from APOGEE, the GALAH DR2, and the GALAH DR2c agree to within 0.07 dex. The lowest values are for GALAH DR2c and the highest are for GALAH DR2. We now



Downloaded from https://academic.oup.com/mnras/article/490/4/5335/5586605 by guest on 07 December 2020

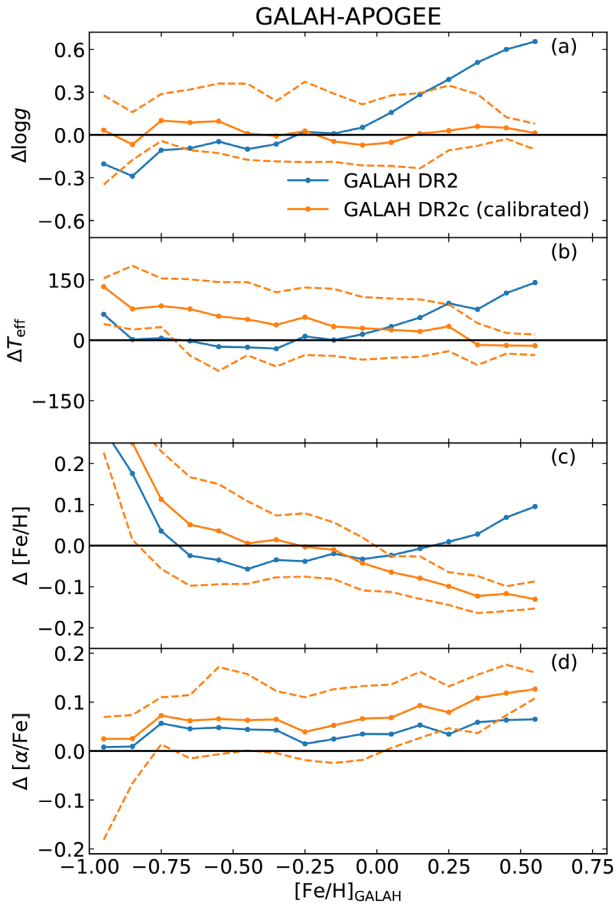


**Figure 11.** Comparison of GALAH DR2 stellar parameters with APOGEE-DR14 stellar parameters. Results corresponding to both uncalibrated and calibrated GALAH DR2 data are shown.

investigate if the metallicity of stars in $5 < R/\mathrm{kpc} < 11$ and $1 < |z|/\mathrm{kpc} < 2$ is really representative of the thick disc metallicity. We show in Table 5 estimates from a mock *Galaxia* sample matched to the GALAH survey, with a thick disc having a mean [M/H] metallicity of −0.18, for stars lying in the same spatial selection. The estimated metallicity is higher by only 0.01 dex compared to the metallicity of the thick disc that was used in the model. This suggests that the metallicity of stars with $5 < R/\mathrm{kpc} < 11$ and $1 < |z|/\mathrm{kpc} < 2$ is indeed close to the actual metallicity of the thick disc but is probably higher by 0.01 dex. Note, GALAH and APOGEE are magnitude-limited surveys, so their samples are not volume complete and this can bias the estimates of the mean metallicity.

We now measure the metallicity of the thick disc more accurately by taking the selection function into account. For this, we fitted a Galactic model to the GALAH DR2c data lying within $5 < R/\mathrm{kpc} < 11$, $0.75 < |z|/\mathrm{kpc} < 3$, $9 < V_{JK} < 14$, and with $0 \leq \texttt{field_id} < 7117$, and having positive rotation, using our importance-sampling framework (Section 3.3).

The fitting procedure gave a mean metallicity of −0.16 with a spread of 0.17 for the thick disc and a mean metallicity of 0.0 for the oldest three thin disc subpopulations. While fitting the model, the spread of the thin disc metallicity with age, and the metallicity of the youngest four thin disc subpopulations was left unchanged as in the Besançon model (Robin et al. 2003). We also assumed that the three oldest thin disc subpopulations (age 3–10 Gyr) have the same mean metallicity. We make these assumptions because we do not make use of the age information in our fitting, and without ages it is difficult to constrain the age metallicity relation. In our fitting, the limited ability to constrain the age metallicity relation comes from the fact that the vertical height of a star is correlated with age. Additionally, the age of the thick disc was assumed to span from 9 to 11 Gyr. We also checked with an age span of 10–12 Gyr for the thick disc and found that it gives the same best-fitting parameters. The slight decrease in the mean metallicity of the thick disc compared to the estimate based on simply measuring the metallicity of stars within $5 < R/\mathrm{kpc} < 11$ and $1 < |z|/\mathrm{kpc} < 2$, is due to the inclusion of stars lying between $2 < |z|/\mathrm{kpc} < 3$ in the fitting process. This suggests that there is a small vertical gradient in the metallicity of the thick disc as found by others previously (Kordopatis et al. 2011; Duong et al. 2018). Note, stars in $2 < |z|/\mathrm{kpc} < 3$ were not included in the former scheme as they could be contaminated with stars from the metal-poor stellar halo and could suffer from volume incompleteness. However, they are included in the later scheme because it takes both these effects into account.

In Fig. 12 we show the mean metallicity as function of Galactocentric radius $R$ for different slices in height $|z|$ for all stars with positive rotation about the Galaxy, which should eliminate star belonging to the halo. Results from APOGEE-DR14 and GALAH DR2c are shown separately. We also plot *Galaxia* predictions from the MP and MR models. The MP model clearly has a thick disc that is too metal poor to fit the observed data for $|z| > 1$ kpc. The new MR model reproduces the GALAH data very well. It also reproduces the APOGEE data very well, except for the slice closest to the mid-plane and the slice furthest from the mid-plane. Compared to GALAH, stars in APOGEE that are close to the mid-plane are metal rich, but the stars progressively become metal poor with increasing height above the mid-plane. These differences could be due to systematics in abundances between the two surveys, but could also be due to the different selection function of the surveys. The effect of selection function is clearly visible in Fig. 12(f) corresponding to the top most slice ($2 < |z|/\mathrm{kpc} < 3$). Here, the MR model has a thick disc with a mean metallicity of −0.16. However, the mean metallicity of stars in this slice is −0.2. This is due to two reasons. First, because the metal poor stars are more luminous and are visible furthest in a magnitude-limited survey, we find that this effect decreases the metallicity of thick disc stars in this slice by 0.02 dex. Secondly, the top most slice has a larger contribution from the (metal poor) halo compared to other slices and this contamination decreases the metallicity of stars in this slice by −0.015 dex. Fig. 12 shows that close to the mid-plane there is a strong radial metallicity gradient. As we move away from the mid-plane the gradient diminishes progressively to zero. Close to the plane, a radial gradient of −0.07 (dashed line), as used in the Besançon (MP) and MR models, is roughly consistent with the observed data.

We now study the distribution of metallicity for oscillating giants for which we have spectroscopic metallicities from K2-HERMES (for the K2 stars) and APOGEE (for the *Kepler* stars). In Fig. 13 we show results separately for different campaigns [C1, C6, C4, C7, and *Kepler* (Kep)] and different seismic classes (hRGB, RC, lRGB). Predictions from *Galaxia*-MP (orange) and the new *Galaxia*-MR (green) are shown alongside the observed data (blue). When comparing models to observations we took both the K2GAP (Section 2.1) and the K2-HERMES selection function into account. For *Kepler*, we took the *Kepler* selection function (Section 2.1) into account and assumed that stars with APOGEE metallicties were a random subset of the seismic sample. The *Galaxia*-MP samples have many more metal poor stars with [M/H]$<-0.5$ than

Downloaded from https://academic.oup.com/mnras/article/490/4/5335/5586605 by guest on 07 December 2020

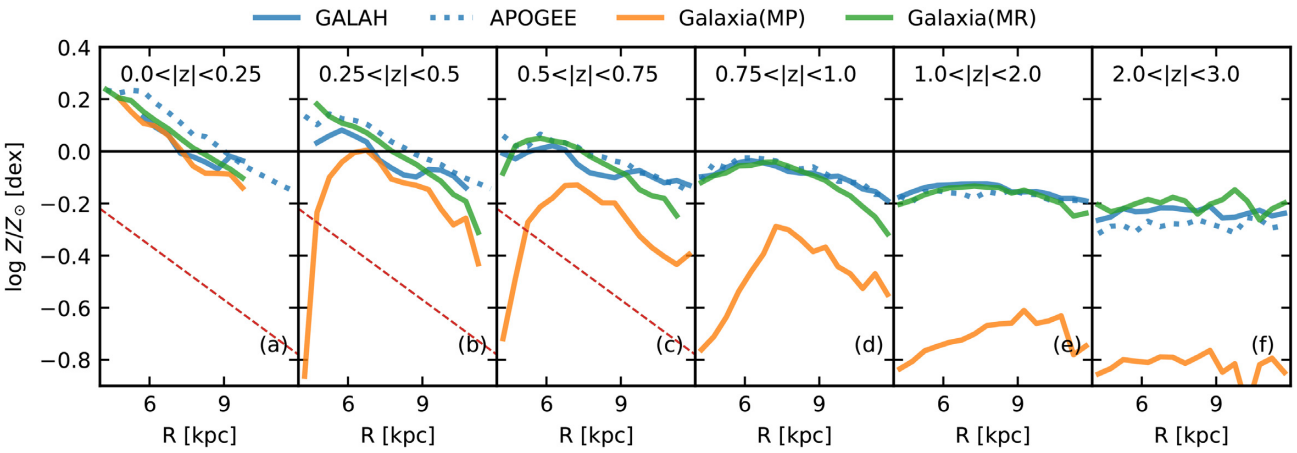


**Figure 12.** Mean metallicity as function of Galactocentric radius $R$ for different slices in height $|z|$ for all stars with positive rotation about the Galaxy. The observed results are from GALAH DR2 (calibrated) and APOGEE-DR14. Selection-function-matched *Galaxia* predictions based on two different Milky Way models (the old MP model and the new MR model) are also shown. The metallicity profile has a gradient close to the plane but is flat above the plane. The dashed line for reference denotes [M/H] with a radial gradient of $-0.07$ dex kpc$^{-1}$.

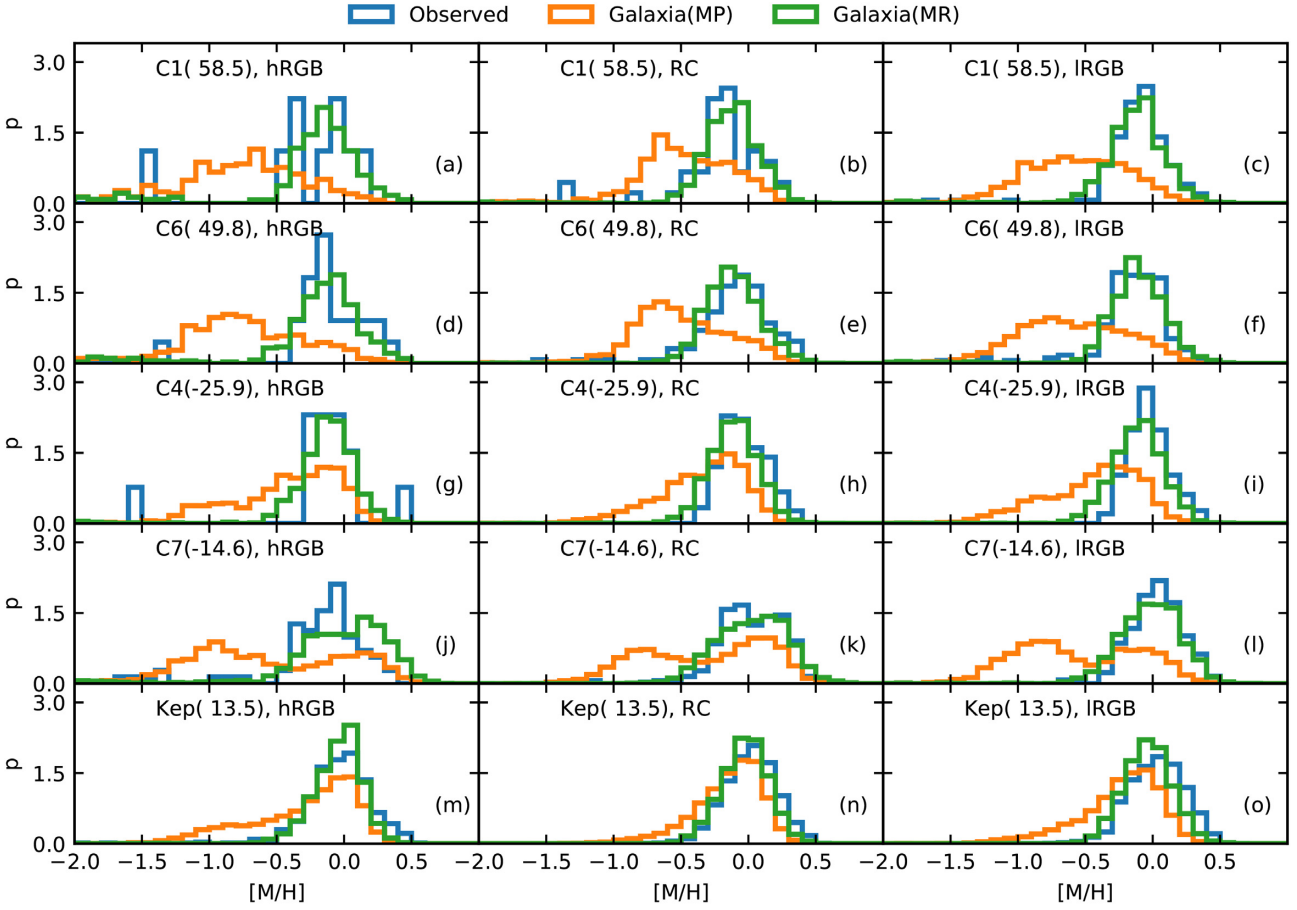


**Figure 13.** The distribution of metallicity[M/H] for RGB and red clump stars with seismic detections from K2 campaigns C1, C4, C6, C7, and *Kepler*. The Galactic latitude for the centre of each campaign is enclosed in parenthesis. The left-hand panels (a, d, g, j, m) show high-luminosity RGB stars, middle panels (b, e, h, k, n) show red clump stars, and right-hand panels (c, f, i, l, o) show low-luminosity RGB stars. Observed data are compared against predictions from theoretical models, the default model of *Galaxia*-MP, which has a metal poor thick disc and the new model MR, which has a more metal rich thick disc. The metallicity for the K2 stars is from the K2-HERMES survey while for the *Kepler* stars we adopt APOGEE-DR14 metallicities.

Downloaded from https://academic.oup.com/mnras/article/490/4/5335/5586605 by guest on 07 December 2020

the observed stars. In some panels a double-peaked distribution can also be seen with one of the peaks being at –0.78, corresponding to the metallicity of the thick disc in the model. The new *Galaxia*-MR model, which has a metal rich thick disc ($\langle$[M/H]$\rangle \sim -0.16$), does not show a bimodal behaviour and its distribution matches very well with observations. However, slight mismatches can be seen for low-latitude campaigns. For RC and lRGB stars in C4 and the *Kepler* field, the *Galaxia*-MR samples are still too metal poor. For hRGB in C7 the *Galaxia*-MR samples are too metal rich.

### 4.2 Constraints from asteroseismology

In this section, we present results making use of the asteroseismic data. We first compare the observed distribution of seismic masses against the predictions of fiducial Galactic models. Next, we restrict our analysis to thick disc stars and assuming reasonable priors on the thick disc parameters, we demonstrate that the asteroseismic scaling relations are fairly accurate. Finally, assuming the scaling relations to be correct we estimate the age of the thick disc.

#### *4.2.1 Comparing observed distribution of seismic masses against predictions from Galactic models*

In Fig. 14, we study the distribution of $\kappa_M$. The order of the panels is the same as in Fig. 13. When comparing models to observations, we take the K2 and the *Kepler* selection functions into account. For hRGB K2 stars, the overall sample size is too small to assess the quality of how well the models match the data. Both models seem to perform equally well. However, for the large hRGB *Kepler* sample we do see that the new model provides a visibly better match. Now turning to the RC stars, we see across all campaigns that the new MR model performs better than the old MP model, which predicts too many stars with $\kappa_M < 1$. Finally, for lRGB stars the MR model is significantly better than the MP model, which predicts too many stars with $\kappa_M < 1.25$.

Having seen the qualitative trends, we now move on to do a quantitative comparison of the observed distributions with predictions from *Galaxia*. Specifically, we want to answer the following questions: (a) does the MR model match the K2 data better than the MP model does, and (b) does the MR model also provide a better match to the *Kepler* data, which had issues with the selection function.

The $\kappa_M$ distributions are in general unimodal. At the most basic level a unimodal distribution over a finite domain can be characterized by a median. We first estimate the medians and then compute the ratio of medians between the observed and predicted distributions, which we show in Table 7. Ideally, we expect the ratio to be close to one, but in previous work based on *Kepler* data, we found the median ratio to be larger than one (1.06).

The new MR model, anchored on GALAH metilicities of the thick disc, is undoubtedly better than the old MP model. For almost all giant classes and campaigns, the median ratio for the new MR model is closer to unity than for the old MP model. The only two exceptions are hRGB for C6 and C7, where the ratio is about 0.85, i.e. the model overpredicts the masses. However, these samples suffer from low number statistics. Additionally for the hRGB stars in C7, we also noticed that the MR model overpredicts the metallicity Fig. 13, and this will lead to overestimation of masses in the MR model.

#### *4.2.2 Testing the accuracy of the asteroseismic mass scaling relation*

The fact that the mass distribution of the new model MR matches the observed seismic masses so well, suggests that the asteroseismic scaling relations are fairly accurate. In the following we will explore this more quantitatively by limiting the analysis to a single Galactic component and imposing reasonable non-seismic priors on its parameters. To do this, we study the mass distribution of stars lying between $1 < |z|/\mathrm{kpc} < 3$. The Galactic model predicts that about 90 per cent of these stars should be thick disc stars, so we can model them as a stellar population characterized by some age distribution and metallicity distribution. We have already shown that the metallicity distribution of this population can be represented by $\mathcal{N}(-0.16, 0.17^2)$. In the following we present several pieces of evidence suggesting that the mean age of this high $|z|$ population should be between 8 and 12 Gyr. First, Fig. 9 shows that stars between $1 < |z|/\mathrm{kpc} < 2$ are enhanced in $\alpha$ element abundances and form a distinct sequence in the abundance space. Using dwarf and subgiants in the solar neighborhood, it has been shown that the stars in the $\alpha$-enhanced sequence are typically older than 10 Gyr (Bensby et al. 2014 fig. 22 and Hayden et al. 2017 fig. 3). Secondly, chemical evolution models predict that $\alpha$-enhanced stars must have formed within the first 1 Gyr of the star formation history of the Milky Way, or else the contribution from Type Ia supernovae would have introduced too much iron and hence brought the value of [$\alpha$/Fe] down (Pagel 2009). When the above fact is combined with fig. 3 from Hayden et al. (2017), which suggest that the oldest thin disc stars (stars not enhanced in [$\alpha$/Fe]) are around 8–10 Gyr old, we reach the conclusion that the $\alpha$-enhanced population must be older than 8 to 10 Gyr. Finally, Kilic et al. (2017) provide one of the most precise and accurate estimates on the mean age of the thick disc using nearby white dwarfs. They estimate the mean thick disc age to be between 9.5 and 9.9 Gyr, with a random uncertainty of about 0.2 Gyr. Hence, based on these observational evidence, a reasonable prior for the mean age of the thick disc is 8–12 Gyr.

To test the asteroseismic mass scaling relation we select the lRGB stars in K2 campaigns C1 and C6 that lie between $1 < |z|/\mathrm{kpc} < 3$. We avoid campaigns C4 and C7 because they point into the Galactic plane and hence lack high $|z|$ stars. We restrict our test to lRGB stars because for these stars there is almost 100 per cent probability both to detect $\nu_{\max}$ and to detect $\Delta\nu$ when a $\nu_{\max}$ has been measured. The distribution of $\kappa_M$ for the lRGB stars is shown in Fig. 15. The distributions of $\kappa_M$ for a stellar population with a metallicity distribution of $\mathcal{N}(-0.16, 0.17^2)$[3] and a mean age of $\tau = 10$ Gyr is also shown alongside, showing a good match to the observed distribution. However, the distribution for the stellar population with $\tau = 7$ Gyr but the same metallicity distribution as before, is shifted too far to the right. Now, to quantify the accuracy of the asteroseismic mass scaling relation (equation 12), we introduce a factor $f_M$, that is multiplied to $\kappa_M$ for stars in the model to get a 'corrected' mass, and then we investigate how close to unity this correction factor is when enforcing that the observed and model mass distributions match.

The posterior distribution of $f_M$ and the age, $\tau$, conditional on our data $D$ is given in Fig. 16. For the mean age of the high $|z|$ population we assume a flat prior in the range 8–12 Gyr. The analysis was done using the importance sampling framework discussed in Section 3.3 and taking the photometric selection function into account. The

[3] $\mathcal{N}(\mu, \sigma^2)$ represents a normal distribution with mean $\mu$ and variance $\sigma^2$.



Downloaded from https://academic.oup.com/mnras/article/490/4/5335/5586605 by guest on 07 December 2020

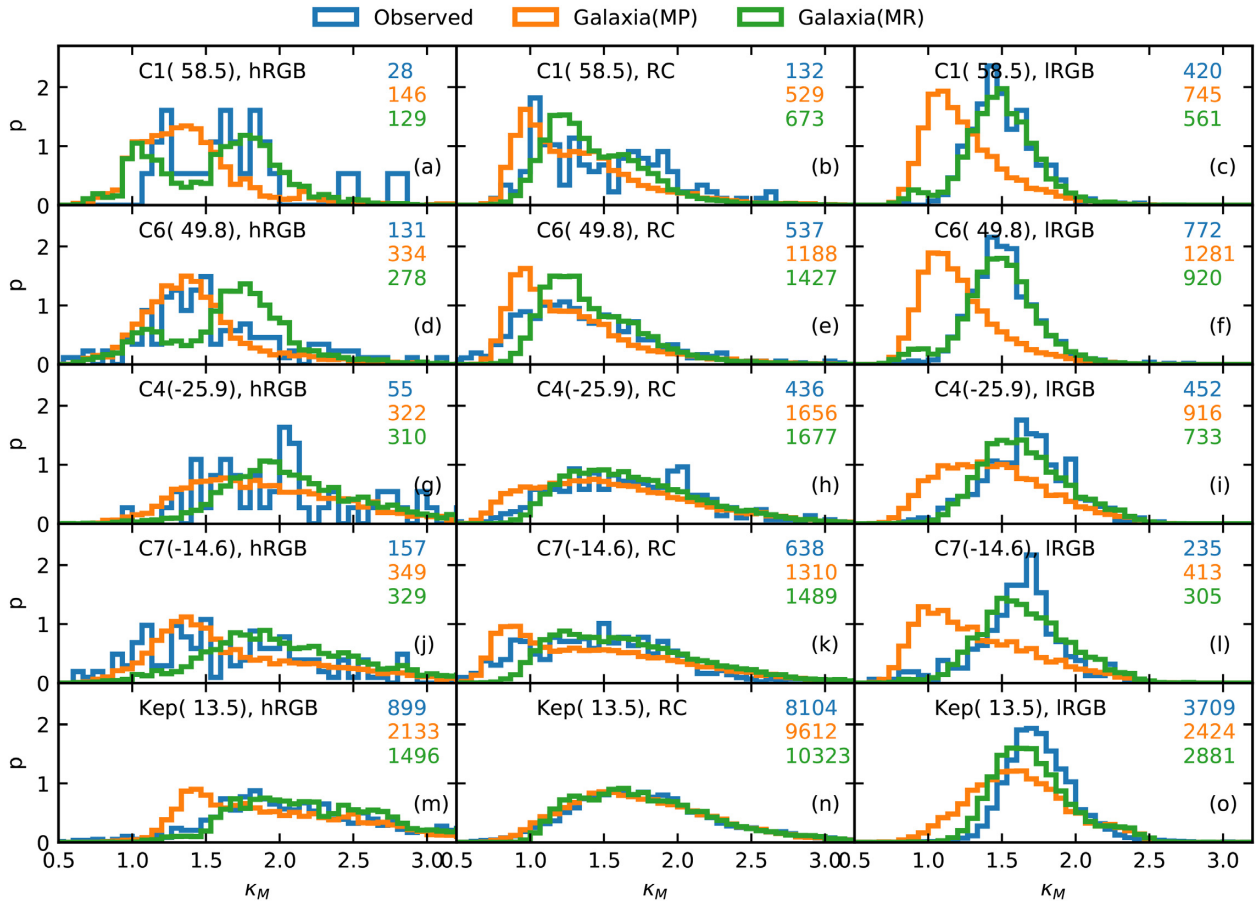


**Figure 14.** The distribution of $\kappa_M$ for RGB and red clump stars for campaigns C1, C4, C6, C7, and *Kepler*. The annotation and order of the panels are the same as in Fig. 13. For each panel, the number of stars in each sample is listed on the right-hand side.

**Table 7.** Ratio of observed (CAN pipeline) median $\kappa_M$ to that predicted by *Galaxia* for different giant classes. Results for two different Galactic models MP (metal poor) and MR (metal rich) are shown. Uncertainties on the computed ratio are also listed.

| | hRGB | | RC | | lRGB | |
|---|---|---|---|---|---|---|
| Campaign | *Galaxia*(MP) | *Galaxia*(MR) | *Galaxia*(MP) | *Galaxia*(MR) | *Galaxia*(MP) | *Galaxia*(MR) |
| 1 | 1.23 ± 0.05 | 1.01 ± 0.04 | 1.15 ± 0.03 | 1.05 ± 0.03 | 1.242 ± 0.009 | 0.992 ± 0.007 |
| 6 | 1.07 ± 0.03 | 0.87 ± 0.02 | 1.11 ± 0.02 | 0.97 ± 0.01 | 1.287 ± 0.007 | 1.002 ± 0.005 |
| 4 | 1.07 ± 0.04 | 0.98 ± 0.04 | 1.11 ± 0.02 | 1.01 ± 0.01 | 1.18 ± 0.01 | 1.027 ± 0.009 |
| 7 | 1.05 ± 0.03 | 0.83 ± 0.03 | 1.07 ± 0.02 | 0.92 ± 0.01 | 1.3 ± 0.01 | 1 ± 0.01 |
| *Kepler* | 1.1 ± 0.01 | 0.96 ± 0.01 | 1.021 ± 0.003 | 1.009 ± 0.003 | 1.086 ± 0.003 | 1.037 ± 0.002 |

figure shows that $f_M$ depends upon $\tau$ and varies between 0.97 and 1.05 for the adopted range of $\tau$. This would translate into a maximum deviation of the $\nu_{\rm max}$ scaling relation (equation 5) of 1–2 per cent if the $\Delta\nu$ scaling relation (equation 5) is true. Or alternatively, that the maximum deviation of the $\Delta\nu$ scaling relation would be about 1 per cent if the $\nu_{\rm max}$ scaling relation is true. Now, if both the $\Delta\nu$ and the $\nu_{\rm max}$ relations are incorrect but conspire to cancel out their inaccuracy when using the mass scaling relation (equation 12), one could in principle have a scenario where large deviations of the $\Delta\nu$ and $\nu_{\rm max}$ relations could be hidden in our mass test. However, this seems not to be the case because when testing the radius scaling relation

$$\frac{R}{R_\odot} = \left(\frac{\nu_{\rm max}}{\nu_{\rm max,\odot}}\right)\left(\frac{\Delta\nu_\odot}{\Delta\nu_\odot}\right)^{-2}\left(\frac{T_{\rm eff}}{T_{\rm eff,\odot}}\right)^{0.5}, \quad (15)$$

which is based on different powers of $\Delta\nu$ and $\nu_{\rm max}$, Zinn et al. (2019) finds agreement between seismic and *Gaia* radii at the 1 per cent level. Hence, in combination these mass and radius scaling relation tests show strong evidence that the individual $\Delta\nu$ and $\nu_{\rm max}$ scaling relations that go into the mass and radius scaling relations are in fact astonishingly accurate.

### 4.2.3 Constraining the age of the thick disc

Having established that the asteroseismic scaling relations are good to a high degree of accuracy, it would seem reasonable to now turn the problem around. Hence, in the following we assume the relations to be true and use the observed values of $\kappa_M$ to estimate the age and metallicity of the thick disc. We do this using the importance sampling framework discussed in Section 3.3. Here, we



Downloaded from https://academic.oup.com/mnras/article/490/4/5335/5586605 by guest on 07 December 2020

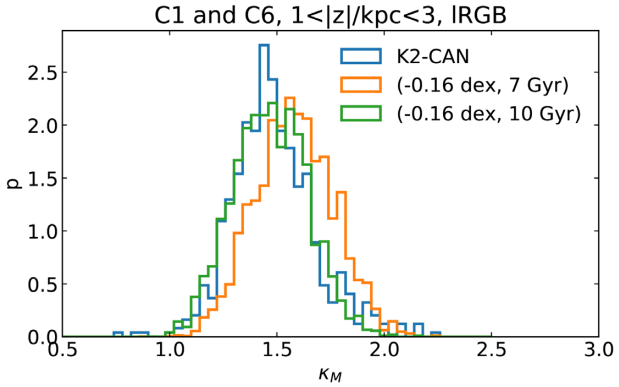


**Figure 15.** The distribution of $\kappa_M$ for lRGB stars in K2 campaigns C1 and C6 that lie between $1 < |z|/\mathrm{kpc} < 3$. Shown alongside are mass distributions corresponding to stellar populations with a Gaussian metallicity distribution and a uniform age distribution (with a width of 2 Gyr). The mean metallicity and the mean age of each stellar population is given in the legend.

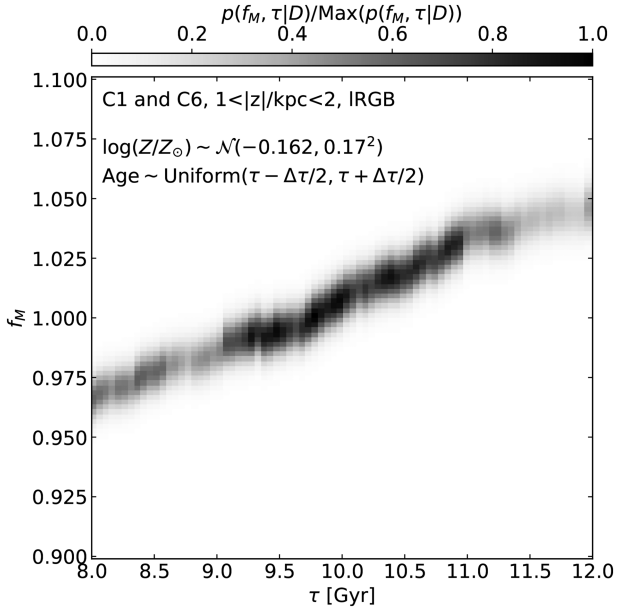


**Figure 16.** The posterior distribution of $f_M$ and mean age of the thick disc $\tau$ obtained using lRGB stars in K2 campaigns C1 and C6 that lie between $1 < |z|/\mathrm{kpc} < 3$. The width $\Delta\tau$ of the age distribution was assumed to be 2 Gyr.

use the FL Galactic model from Table 3 as the base model and reweight it to simulate samples corresponding to different values of the parameters of the model. We compute the likelihood of the observed $\kappa_M$ values given the model for different values of the mean metallicity, $\log Z/Z_\odot$, and mean age for the thick disc. Given the uncertain selection function of the *Kepler* data, only data from the K2 campaigns were used. The results are shown in Fig. 17. We adopted a duration of 2 Gyr for the star formation episode of the thick disc. We also investigated shorter (1 Gyr) and longer (3 Gyr) star formation durations and found that the results were not too sensitive to the exact choice of the duration.

Fig. 17(a) shows the likelihood when considering all giants. Fig. 17(c) shows the likelihood when only lRGB giants are used. It can be seen that when we only consider the asteroseismic information, age is degenerate with metallicity. A decrease in the

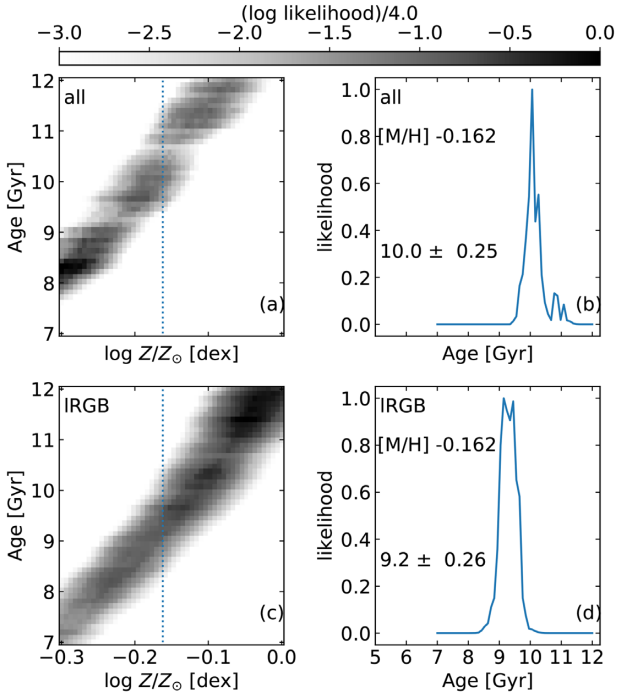


**Figure 17.** (a, c) Likelihood of age and metallicity of the thick disc using asteroseismic information from K2 campaigns C1, C4, C6, and C7. (b–d) The likelihood of thick disc age assuming the thick disc metallicity to be $\log(Z/Z_\odot) = -0.16$, as estimated using the GALAH survey in Table 2. In the top panels, the likelihood is computed using all oscillating giants, while in the bottom panels, only low luminosity giants (Section 3.6) are used.

adopted metallicity by 0.1 dex can decrease the inferred age by about 2 Gyr. Fig. 17(a) shows that a metal poor thick disc cannot be old. For example, a thick disc with $\log Z/Z_\odot = -0.3$ will have an age of about 8 Gyr and would be even younger if it was more metal poor (such as the old MP model). For a star with a given mass, the decrease in age with a decrease in metallicity is expected because a low-metallicity star evolves much faster along the HR diagram, compared to a high-metallicity star.

Figs 17(b) and (d) show the likelihood as a function of age when we fix the metallicity to −0.16 as suggested by the spectroscopic data. Using all giants we get a mean age of 10 Gyr, if only lRGB stars are used we obtain 9.2 Gyr. Both estimates are consistent with the traditional idea of an old thick disc.

## 5 DISCUSSION AND CONCLUSIONS

Asteroseismology can provide ages for giant stars and hence is a promising tool for studying Galactic structure and evolution. However, it has proven to be difficult to check the accuracy of the ages and masses estimated by asteroseismology, due to the shortage of independent estimates of mass and age. Population synthesis based Galactic models, provide an indirect way to validate the asteroseismic estimates. However, previous studies using the *Kepler* mission revealed that the models predict too many low mass stars as compared to observed mass distributions, raising doubts on the accuracy of the asteroseismic estimates, the Galactic models, and/or the selection function. In this paper, we revisit this important problem by analysing asteroseismic data from the K2 mission, which has a well-defined selection function. For the first time, we show that if the metallicity distribution in the Galactic models is

Downloaded from https://academic.oup.com/mnras/article/490/4/5335/5586605 by guest on 07 December 2020

updated to measurements from recent spectroscopic surveys, the distribution of asteroseismic masses is in good agreement with the model predictions. Using thick disc stars we show that the asteroseismic mass scaling relation for low-luminosity red giants should be accurate to at least 5 per cent. This is in agreement with findings of Brogaard et al. (2018) who tested the seismic relations using three eclipsing binary systems.

We identify three main factors, which, if not taken into account, can lead to discrepancies between observed asteroseismic masses and model predictions. First, in addition to age, the mass distribution of giant stars in a stellar population is very sensitive to its metallicity, hence it is important to get the metallicity distribution of the various Galactic components in a model to agree with observations. Secondly, certain Galactic components are significantly enhanced in abundance of $\alpha$ elements and this should be taken into account, either directly by using $\alpha$ enhanced isochrones, or indirectly by increasing the effective metallicity of the solar scaled isochrones. Thirdly, the $\Delta\nu$ scaling relation is not strictly valid and there exists theoretically motivated corrections, which should be applied. It was already shown in a previous study (Sharma et al. 2016) that the correction is such that it helps to reduce the mass discrepancy.

Using a forward modelling approach, where we take the Besançon Galactic model as a prior, we fit for the effective metallicity $Z$ (taking $\alpha$ enhancement into account) of the thin and the thick disc using the GALAH data. We find the mean $\log Z/Z_{\odot}$ of the thin disc to be 0.0 and that of the thick disc to be $-0.16$ (with a dispersion of 0.17, see Table 5). This is in good agreement with data from the APOGEE survey. This is a significant revision for the thick disc from a value of [Fe/H] $= -0.78$ as used in the Besançon model. An increase of about 0.14 dex in $\log Z/Z_{\odot}$ is due to taking the $\alpha$ enhancement into account, but about 0.5 dex is due to revision of [Fe/H]. For example, if we consider stars in $5 < R/\mathrm{kpc} < 7$ and $1 < |z|/\mathrm{kpc} < 2$, which mostly come from the thick disc, both GALAH and APOGEE suggest a mean [Fe/H] $\sim -0.30$ for the thick disc.

Using a forward modelling approach, we also fit for the age of the thick disc using the asteroseismic data. We find the mean age to be about $9.2 - 10 \pm 0.25$ Gyr (redshift of about 1.6), which is broadly consistent with the idea of the thick disc being old and formed early on in the history of the Galaxy. What exactly do we mean by thick disc? Traditionally the thick disc was identified as the component with higher scale height in the solar annulus. Observations also suggest the thick disc to be distinct from the thin disc in elemental abundances. Two sequences $\alpha_+$ and $\alpha_o$ can be seen in the ([$\alpha$/Fe], [Fe/H]) plane, with the former (having higher [$\alpha$/Fe]) being the thick disc and the later the thin disc. New results (Bensby et al. 2011; Bovy et al. 2012; Mackereth et al. 2017; Xiang et al. 2017) suggest that the scale length of the $\alpha_+$ sequence is shorter than that of the $\alpha_o$ sequence. Chemical evolution models require the $\alpha_+$ sequence to be old. In our forward modelling we do not identify the thick disc using elemental abundances. Instead the thick disc is indirectly identified by our prior for the spatial distribution of thin and thick disc stars. In the model, stars with $|z| > 1$ kpc are dominated by thick disc. The majority of the thick disc stars in our data come from the high-latitude campaigns C1 and C6, and these stars have Galactocentric radius similar to that of the Sun. So our thick disc metallicity and age measurements are representative of the properties of the stellar population that roughly dominates in the region $|z|/\mathrm{kpc} > 1$ and $6 < R/\mathrm{kpc} < 10$.

Our thick disc age estimate is consistent with previous studies that estimated the mean age independent of asteroseismology. For example, it is consistent with results by Bensby, Feltzing & Lundström (2003) who estimate the age to be $11.2 \pm 4.3$ using F and G dwarfs. It is consistent with Xiang et al. (2017) from LAMOST using main-sequence turn-off stars and subgiants, where they show that stars with, $|z| > 1$ kpc have a median age close to 10 Gyr and are $\alpha$ enhanced. It is consistent with results by Mackereth et al. (2017) from APOGEE using giants, where they show that $\alpha$ enhanced stars have significantly larger scale height and their mean age is close to or larger than 10 Gyr. However, the age estimates in Mackereth et al. (2017) are anchored on the asteroseismic age scale. Finally, our estimate ($9.2 - 10 \pm 0.25$ Gyr) is in excellent agreement with estimates of Kilic et al. (2017) of $9.5 - 9.9 \pm 0.2$ Gyr using white dwarfs, an estimate that is very accurate and independent of both asteroseismology and the isochrones. Note, our quoted systematic error on the age of the thick disc does not include errors due to systematics offsets in spectroscopic metallicities. Based on our likelihood maps one can update the age for any given thick-disc metallicity. In general, if the thick-disc metallicity is lowered (or increased) the thick disc will become younger (or older).

Although we find that the observed mass distributions are in good agreement with predictions by Galactic models, some small unexplained differences do remain. For lRGB, the predicted mean of the mass distributions for K2 campaign C4 and *Kepler* are higher by about 3 per cent. We also see differences in metallicity distributions for these samples and this could potentially be responsible for the mass differences. For hRGB and red clumps, the mean predicted mass is lower than observed, for campaigns C6 and C7. This could be due to imperfections in the model, but could also be related to the fact that the detection of $\Delta\nu$ is not complete for these stars.

We presented the selection function for four K2 campaigns and discussed detection biases associated with the K2 data, which should be taken into account when using the K2 data. The probability to detect $\nu_{\mathrm{max}}$ varies with both $\nu_{\mathrm{max}}$ and apparent magnitude. Low-luminosity stars have lower oscillation amplitudes and cannot be detected at fainter magnitudes. Even after we account for the effect of oscillation amplitude and apparent magnitude, comparison with Galactic models show that the overall detection rate for $\nu_{\mathrm{max}}$ is about 72 per cent. Using a deep-learning-based pipeline improves the detection rate to 78 per cent, which is still quite low. It is not yet clear why the detection rate is low. It could be that certain types of stars (e.g. red clumps or metal poor stars) have lower than expected oscillation amplitudes, or it could be an unknown instrumental effect, or even a problem with the Galactic model. There are also biases related to detecting $\Delta\nu$ in the K2 data. The probability to detect $\Delta\nu$ has a strong dependence on $\nu_{\mathrm{max}}$, it is less than 1 for $\nu_{\mathrm{max}} < 50\,\mu$Hz, but is otherwise close to 1. Significant campaign to campaign differences are also seen, which needs further investigation. To take the detection biases into account, we propose to split up the stars into different giant classes based on their detection probabilities.

Using the seismic sample, we find that the stellar parameters for giants in GALAH DR2, which are based on the data-driven *The Cannon* scheme, have systematic differences with respect to estimates based on the model-driven SME scheme, which is anchored to seismic $\nu_{\mathrm{max}}$ values. Differences are most significant for stars with [Fe/H] $> 0$. We provide analytical functions to correct for them. The reason for the systematic offsets is because the giants in the training set used by *The Cannon* were dominated by non-seismic giants. In the absence of a seismic $\nu_{\mathrm{max}}$, the SME gives biased results. SME with *Gaia* DR2 parallaxes as prior alleviates this problem, however, *Gaia* DR2 parallaxes were not available at the time of publication of GALAH DR2.

In near future, we will have a much larger sample of stars with asteroseismology from both the K2 and the TESS (Campante et al.

Downloaded from https://academic.oup.com/mnras/article/490/4/5335/5586605 by guest on 07 December 2020

2016; Schofield et al. 2019) missions. This will allow us to fit more detailed models of our Galaxy than done here. Specifically, we can study the properties of the stellar populations as a function of age with much finer age resolution. Future, spectroscopic surveys, such as the second phase of GALAH, 4MOST (de Jong et al. 2016), WEAVE (Dalton et al. 2018), and SDSSV (Kollmeier et al. 2019), will also produce large samples of stars with age estimates purely from spectroscopy, based on main-sequence turn-off and subgiant stars or based on giants making use of the age information encoded in carbon and nitrogen abundances. Asteroseismology in this regard is going to play a crucial role by providing independent age estimates.

## ACKNOWLEDGEMENTS

SS is funded by University of Sydney Senior Fellowship made possible by the office of the Deputy Vice Chancellor of Research, and partial funding from Bland-Hawthorn's Laureate Fellowship from the Australian Research Council (ARC). DS is the recipient of an ARC Future Fellowship (project number FT1400147).

JBH is supported by an ARC Laureate Fellowship (FL140100278). MJH is supported by an ASTRO-3D Fellowship. SB and KL acknowledge funds from the Alexander von Humboldt Foundation in the framework of the Sofja Kovalevskaja Award endowed by the Federal Ministry of Education and Research. KL acknowledges funds from the Swedish Research Council (Grant nr. 2015-00415_3) and Marie Sklodowska Curie Actions (Cofund Project INCA 600398). JK, KC, and TZ acknowledge financial support from the Slovenian Research Agency (research core funding No. P1-0188). DMN was supported by the Allan C. and Dorothy H. Davis Fellowship. JZ acknowledges support from NASA grants 80NSSC18K0391 and NNX17AJ40G. The GALAH Survey is supported by the ARC Centre of Excellence for All Sky Astrophysics in 3 Dimensions (ASTRO 3D), through project number CE170100013. This work has made use of data acquired through the Australian Astronomical Observatory, under programmes: GALAH and K2-HERMES.

This work has made use of data from the European Space Agency (ESA) mission *Gaia* (https://www.cosmos.esa.int/gaia), processed by the *Gaia* Data Processing and Analysis Consortium (DPAC, https://www.cosmos.esa.int/web/gaia/dpac/consortium). Funding for the DPAC has been provided by national institutions, in particular the institutions participating in the *Gaia* Multilateral Agreement.

This work has made use of data from SDSS(Sloan Digital Sky Survey)-III. Funding for SDSS-III has been provided by the Alfred P. Sloan Foundation, the Participating Institutions, the National Science Foundation, and the U.S. Department of Energy Office of Science. The SDSS-III web site is http://www.sdss3.org/.

## REFERENCES

Anders F. et al., 2017, A&A, 597, A30
Bensby T., Feltzing S., Lundström I., 2003, A&A, 410, 527
Bensby T., Alves-Brito A., Oey M. S., Yong D., Meléndez J., 2011, ApJ, 735, L46
Bensby T., Feltzing S., Oey M. S., 2014, A&A, 562, A71
Bland-Hawthorn J. et al., 2018, MNRAS, 486, 1167
Boeche C. et al., 2013, A&A, 559, A59
Boeche C. et al., 2014, A&A, 568, A71
Borucki W. J. et al., 2010, Science, 327, 977
Bovy J., Rix H.-W., Liu C., Hogg D. W., Beers T. C., Lee Y. S., 2012, ApJ, 753, 148
Bressan A., Marigo P., Girardi L., Salasnich B., Dal Cero C., Rubele S., Nanni A., 2012, MNRAS, 427, 127
Brogaard K. et al., 2018, MNRAS, 476, 3729
Brown T. M., Gilliland R. L., Noyes R. W., Ramsey L. W., 1991, ApJ, 368, 599
Brown T. M., Latham D. W., Everett M. E., Esquerdo G. A., 2011, AJ, 142, 112
Buder S. et al., 2018, MNRAS, 478, 4513
Campante T. L. et al., 2016, ApJ, 830, 138
Casagrande L. et al., 2014, ApJ, 787, 110
Casagrande L. et al., 2016, MNRAS, 455, 987
Chaplin W. J., Miglio A., 2013, ARA&A, 51, 353
Chaplin W. J. et al., 2011a, ApJ, 732, 54
Chaplin W. J. et al., 2011b, Science, 332, 213
Chen Y., Girardi L., Bressan A., Marigo P., Barbieri M., Kong X., 2014, MNRAS, 444, 2525
Chen Y., Bressan A., Girardi L., Marigo P., Kong X., Lanza A., 2015, MNRAS, 452, 1068
Ciardi D. R. et al., 2011, AJ, 141, 108
Dalton G. et al., 2018, Proc. SPIE Conf. Ser. Vol. 10702, Ground-Based and Airborne Instrumentation for Astronomy VII. SPIE, Bellingham, p. 107021B
de Jong R. S. et al., 2016, Proc. SPIE Conf. Ser. Vol. 9908, Ground-Based and Airborne Instrumentation for Astronomy VI. SPIE, Bellingham, p. 99081O
De Silva G. M. et al., 2015, MNRAS, 449, 2604
Duong L. et al., 2018, MNRAS, 476, 5216
Gaia Collaboration, 2016, A&A, 595, A1
Gaia Collaboration, 2018, A&A, 616, A1
Gilmore G., Wyse R. F. G., Jones J. B., 1995, AJ, 109, 1095
Girardi L., Groenewegen M. A. T., Hatziminaoglou E., da Costa L., 2005, A&A, 436, 895
Hayden M. R. et al., 2014, AJ, 147, 116
Hayden M. R. et al., 2015, ApJ, 808, 132
Hayden M. R., Recio-Blanco A., de Laverny P., Mikolaitis S., Worley C. C., 2017, A&A, 608, L1
Hon M., Stello D., Yu J., 2018, MNRAS, 476, 3233
Howell S. B. et al., 2014, PASP, 126, 398
Huber D., Stello D., Bedding T. R., Chaplin W. J., Arentoft T., Quirion P.-O., Kjeldsen H., 2009, Commun. Asteroseismol., 160, 74
Jenkins J. M. et al., 2010, ApJ, 713, L120
Kallinger T. et al., 2010, A&A, 522, A1
Kallinger T. et al., 2014, A&A, 570, A41
Kilic M., Munn J. A., Harris H. C., von Hippel T., Liebert J. W., Williams K. A., Jeffery E., DeGennaro S., 2017, ApJ, 837, 162
Kjeldsen H., Bedding T. R., 1995, A&A, 293, 87
Kollmeier J. A. et al., 2019, BAAS, 51, 274
Kordopatis G. et al., 2011, A&A, 535, A107
Kos J. et al., 2017, MNRAS, 464, 1259
Mackereth J. T. et al., 2017, MNRAS, 471, 3057
Majewski S. R. et al., 2017, AJ, 154, 94
Martell S. L. et al., 2017, MNRAS, 465, 3203
Miglio A. et al., 2009, A&A, 503, L21
Miglio A. et al., 2013, MNRAS, 429, 423
Ness M., Hogg D. W., Rix H.-W., Ho A. Y. Q., Zasowski G., 2015, ApJ, 808, 16
Pagel B. E. J., 2009, Nucleosynthesis and Chemical Evolution of Galaxies, 2nd edn. Cambridge Univ. Press, Cambridge
Paxton B., Bildsten L., Dotter A., Herwig F., Lesaffre P., Timmes F., 2011, ApJS, 192, 3
Paxton B. et al., 2013, ApJS, 208, 4
Piskunov N., Valenti J. A., 2017, A&A, 597, A16
Robin A. C., Haywood M., Creze M., Ojha D. K., Bienayme O., 1996, A&A, 305, 125
Robin A. C., Reylé C., Derrière S., Picaud S., 2003, A&A, 409, 523
Rodrigues T. S. et al., 2017, MNRAS, 467, 1433
Salaris M., Cassisi S., 2005, Evolution of Stars and Stellar Populations. John Wiley & Sons, Chichester

Downloaded from https://academic.oup.com/mnras/article/490/4/5335/5586605 by guest on 07 December 2020

Schlegel D. J., Finkbeiner D. P., Davis M., 1998, ApJ, 500, 525
Schofield M. et al., 2019, ApJS, 241, 12
Sharma S., Bland-Hawthorn J., Johnston K. V., Binney J., 2011, ApJ, 730, 3
Sharma S. et al., 2014, ApJ, 793, 51
Sharma S., Stello D., Bland-Hawthorn J., Huber D., Bedding T. R., 2016, ApJ, 822, 15
Sharma S., Stello D., Huber D., Bland-Hawthorn J., Bedding T. R., 2017, ApJ, 835, 163
Sharma S. et al., 2018, MNRAS, 473, 2004
Sheinis A. et al., 2015, J. Astron. Telesc. Instrum. Syst., 1, 035002
Silva Aguirre V. et al., 2018, MNRAS, 475, 5487
Soubiran C., Bienaymé O., Siebert A., 2003, A&A, 398, 141
Stello D. et al., 2011, ApJ, 737, L10
Stello D. et al., 2013, ApJ, 765, L41
Stello D. et al., 2015, ApJ, 809, L3
Stello D. et al., 2017, ApJ, 835, 83
Tang J., Bressan A., Rosenfield P., Slemer A., Marigo P., Girardi L., Bianchi L., 2014, MNRAS, 445, 4287
Townsend R. H. D., Teitler S. A., 2013, MNRAS, 435, 3406
Ulrich R. K., 1986, ApJ, 306, L37
Wittenmyer R. A. et al., 2018, AJ, 155, 84
Xiang M. et al., 2017, ApJS, 232, 2
Zinn J. C., Pinsonneault M. H., Huber D., Stello D., Stassun K., Serenelli A., 2019, preprint (arXiv:1910.00719)

[1]*Sydney Institute for Astronomy, School of Physics, The University of Sydney, Sydney, NSW 2006, Australia*
[2]*ARC Centre of Excellence for All Sky Astrophysics in Three Dimensions (ASTRO-3D), Canberra, ACT 2611, Australia*
[3]*School of Physics, University of New South Wales, Sydney, NSW 2052, Australia*
[4]*Stellar Astrophysics Centre, Department of Physics and Astronomy, Aarhus University, DK-8000 Aarhus C, Denmark*
[5]*Department of Astronomy, The Ohio State University, Columbus, OH 43210, USA*
[6]*Institute of Astrophysics, University of Vienna, Türkenschanzstrasse 17, Vienna A-1180, Austria*
[7]*Research School of Astronomy & Astrophysics, Australian National University, Canberra, ACT 2611, Australia*
[8]*Max Planck Institute for Astronomy (MPIA), Koenigstuhl 17, D-69117 Heidelberg, Germany*
[9]*Department of Physics & Astronomy, Macquarie University, Sydney, NSW 2109, Australia*
[10]*INAF, Vicolo dell'Osservatorio, 5, 35122, Padova, PD, Italy*
[11]*Faculty of Mathematics and Physics, University of Ljubljana, Jadranska 19, 1000 Ljubljana, Slovenia*
[12]*Department of Physics and Astronomy, Uppsala University, Box 516, SE-751 20 Uppsala, Sweden*
[13]*Centre for Astrophysics, University of Southern Queensland, Toowoomba, Queensland 4350, Australia*
[14]*Research Centre in Astronomy, Astrophysics & Astrophotonics, Macquarie University, Sydney, NSW 2109, Australia*
[15]*Institute for Astronomy, University of Hawai'i, 2680 Woodlawn Drive, Honolulu, HI 96822, USA*
[16]*SETI Institute, 189 Bernardo Avenue, Mountain View, CA 94043, USA*
[17]*Stellar Astrophysics Centre, Department of Physics and Astronomy, Aarhus University, Ny Munkegade 120, DK-8000 Aarhus C, Denmark*
[18]*International Centre for Radio Astronomy Research (ICRAR), The University of Western Australia, 35 Stirling Highway, Crawley, WA 6009, Australia*
[19]*Institute for Advanced Study, Princeton, NJ 08540, USA*
[20]*Department of Astrophysical Sciences, Princeton University, Princeton, NJ 08544, USA*
[21]*Observatories of the Carnegie Institution of Washington, 813 Santa Barbara Street, Pasadena, CA 91101, USA*
[22]*Department of Physics and Astronomy, The Johns Hopkins University, Baltimore, MD 21218, USA*

This paper has been typeset from a TEX/LATEX file prepared by the author.

Downloaded from https://academic.oup.com/mnras/article/490/4/5335/5586605 by guest on 07 December 2020